# The Capricorn Orogen magnetotelluric (MT) transect

by

G Heinson[1], G Boren[1], J Ross[1], J Campanya[1], S Thiel[1], and K Selway[1]

## Introduction

In April and May 2010, deep reflection-seismic data were collected along three lines in the Capricorn Orogen, funded through the Western Australian Government's Royalties for Regions Exploration Incentive Scheme (EIS) and the Australian Federal Government's National Earth Science Infrastructure Program (AuScope). The main objectives of these seismic lines were to image:

1. the overall structure and dip of the suture between the Yilgarn Craton and Gascoyne Province (Errabiddy Shear Zone)
2. the depth and shape of the Minnie Creek batholith
3. the nature of reactivated Fortescue Group growth faults in the southern Pilbara
4. the dip of the major faults that mark the boundary between the Pilbara Craton and the Ashburton Basin
5. the deep crustal structure of the Ashburton Basin
6. the deep crustal structure of the Edmund and Collier Basins, and the nature of major growth faults in these basins; e.g. the Talga Fault.

From October to November 2010, a magnetotelluric (MT) survey was conducted along the same transects as the Capricorn seismic lines. Broadband (200 – 0.005 Hz) MT sites were collected every 5 km, and long-period (0.1 – 0.0001 Hz) MT sites every 15 km. In total, 116 broadband and 40 long-period sites were collected over the three transects, spanning approximately 500 km. Like the seismic survey, the MT line was divided into three sections, denoted 10GA–CP1, 10GA–CP2, and 10GA–CP3. The MT results presented in this paper complement earlier long-period MT measurements (Fig. 1) conducted along similar transects by Selway et al. (2009).

There are a number of aspects of MT measurements that make them very complementary to seismic methods.

1. MT signals have different depth penetrations, depending on frequency and on the resistivity of earth materials. The approximate depth of signal penetration into the Earth is known as the skin-depth. The skin-depth increases as frequencies decrease; skin-depth also increases as the resistivity increases.
2. The measurements are vector, which means they indicate the preferred orientation of electric current flow. Thus, MT measurements can delineate the dimensionality of Earth structures, and are sensitive to both lateral and vertical changes in geology.
3. MT measurements are sensitive to the volumetric properties of the crust and mantle, rather than being sensitive to boundaries. The primary physical property measured is electrical conductivity or its reciprocal, resistivity, and this can have changes of six of more orders of magnitude.
4. The MT method does not require an artificial source field, as the signals are all naturally occurring. Thus, the method measures just with receivers, making MT surveys relatively cheap to undertake.

The principal objectives of the MT survey were to complement the seismic reflection profiles, and to indicate any primary changes in electrical resistivity relating to the six objectives listed previously.

## MT measurements

The magnetotelluric (MT) method has been in use for about 50 years, and is now a common technique used to analyse regional 2D and 3D transects (e.g. Simpson and Bahr, 2005). The principal objective of any MT survey is to measure variations in the electric field (E) and magnetic field (B) as time series (Figs 2 and 3).

Magnetic fields are measured as a time series using a magnetometer. These are vector measurements, oriented

[1] Centre for Tectonics, Resources and Exploration, University of Adelaide, Adelaide, SA 5005.

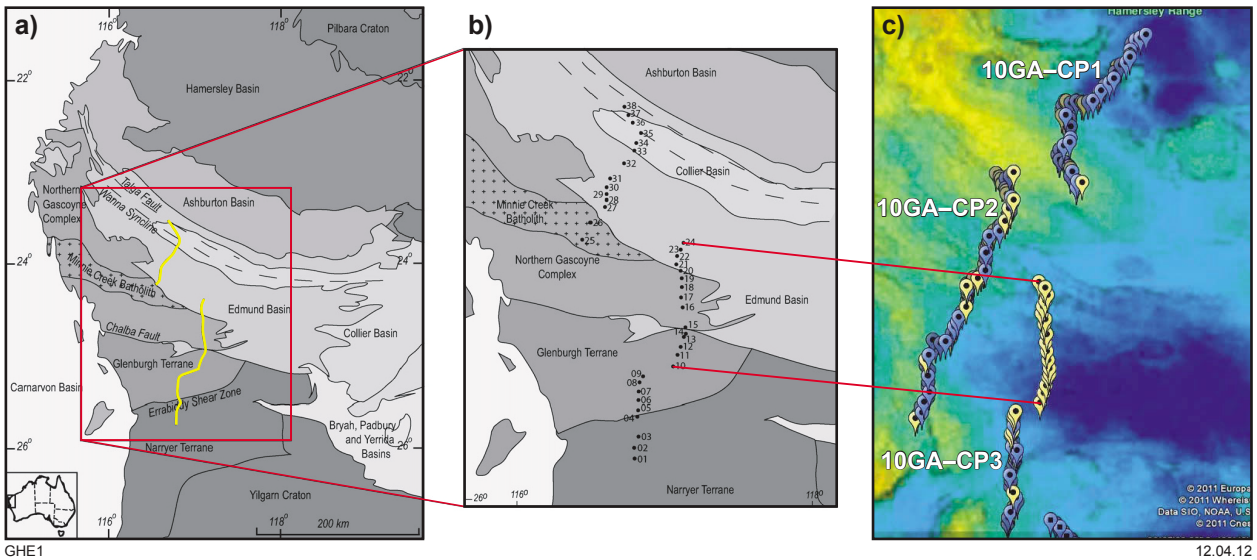


**Figure 1. Profile map of survey: (a) regional scale geology, with survey lines from Selway et al. (2009), marked in yellow; (b) more detailed survey geology from Selway et al. (2009); (c) new broadband MT sites (blue) and long-period MT sites (yellow) plotted on top of a Bouguer gravity map of the region. The locations of the Selway et al. (2009) sites (which were long-period MT) are also shown. New sites were collected along lines 10GA–CP1, 10GA–CP2, and 10GA–CP3.**

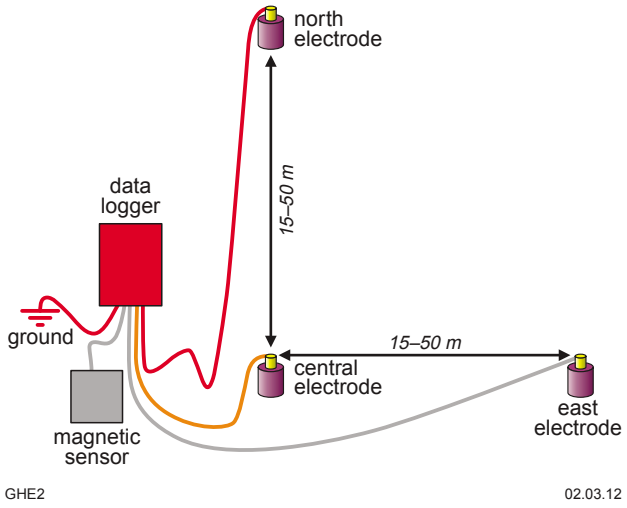


**Figure 2. Typical layout of MT instrumentation.**

in the direction of the sensor alignment. For broadband measurements, induction coils (LEMI120; <http://www.lemisensors.com/?q=lemi_120>) with the highest sensitivity, between 1000 and 0.001 Hz, were used. Only the two horizontal components, north and east orientations, are recorded ($B_x$, $B_y$).

For long-period measurements, a three-component fluxgate sensor (MAG03; <http://www.gmw.com/magnetic_measurements/Bartington/Mag-03.html>) was used, with sensitivity between about 0.1 Hz and DC. These three components are aligned north, east, and vertical ($B_x$, $B_y$, $B_z$).

The electric field is the voltage difference measured between two grounded electrodes, and is given as the voltage gradient (volts per metre; V/m). Typically, offsets are measured in microvolts (mV). Such measurements are vector in that they have both magnitude and direction; generally, electric field dipoles are established with one pair of electrodes orientated north–south ($E_x$), and the other pair oriented west–east ($E_y$).

Note that for the MT method, the important aspect of these magnetic and electric fields is that the fields change with time. The magnetic field changes are primarily due to external effects: at high frequencies (>1 Hz), the source fields are due to lightning strikes around the world, whereas at lower frequencies (<0.1 Hz), the source field are due to the interaction of the Earth's magnetic field with solar winds emanating from the sun. The bandwidth of 1 – 0.1 Hz is known as the dead-band, which typically contains little natural field signal.

The fundamental relationship linking the electric and magnetic fields in the frequency domain is given by the following equation.

$$\begin{pmatrix} E_x \\ E_y \end{pmatrix} = \begin{pmatrix} Z_{xx} & Z_{xx} \\ Z_{xx} & Z_{xx} \end{pmatrix} \begin{pmatrix} B_x \\ B_y \end{pmatrix} \quad (1)$$

In this equation, the matrix components $B_x$ and $B_y$ are the horizontal magnetic fields in the north ($B_x$) and east ($B_y$) directions, and can be considered, at first order, as input or source fields. The two horizontal electric-field components $E_x$ and $E_y$ are the equivalent orientations of the electric field, and are essentially the response of the Earth to inducting fields. Finally, the matrix [Z] is the impedance tensor, which contains information of the Earth as a filter, dependent primarily on electrical resistivity.

For a one-dimensional (1D) layered Earth, the impedance tensor is quite simple, with $Z_{xx} = Z_{yy} = 0$, and $Z_{xy} = -Z_{yx}$. Thus, the orthogonal components of the electric and magnetic fields are linked, and these responses can be written in terms of both an apparent resistivity, $\rho_a$ (in ohm.m, or Ωm), as

$$\rho_a = \frac{0.2}{f}\left|\frac{E_x}{B_y}\right|^2 \quad (2)$$

and a phase angle (which is essentially the phase lag between the electric and magnetic fields), given by:

$$\phi = \tan^{-1}\left(\frac{E_x}{B_y}\right) \quad (3)$$

In these equations, $f$ is the frequency of the signal.

For Earth structures that are relatively two-dimensional (2D) in that they change in electrical properties with depth and in one horizontal orientation, the impedance tensor [Z] can be mathematically rotated so that the observed fields are effectively resampled in directions parallel and perpendicular to the strike of the 2D geology; that is, $Z_{xx} = Z_{yy} = 0$, but $Z_{xy} \neq Z_{yx}$. In this case, the orientation of the fields can be defined as two modes: the TE mode, with the electric field parallel to the geological strike causing a resistivity variation; and the TM mode, in which the electric field is perpendicular to the strike of the geology. In many surveys, the TM mode is the most important, as the flow of electric currents across boundaries produces significant changes in apparent resistivity.

In many cases, the Earth is truly three-dimensional (3D) in that the electrical resistivity varies in both horizontal directions and vertically. In this case, $Z_{xx} \neq Z_{yy} \neq Z_{xy} \neq Z_{yx}$, and modelling is very difficult. The Earth may be anisotropic on a small scale; that is, a single piece of crust may conduct electricity better in one orientation than others.

The apparent resistivity and phase are measured at a wide range of frequencies, which translates to a wide range of depths and distances. The apparent resistivity can be considered as a weighted average of the resistivities to the skin-depth.

The skin-depth equation is given by:

$$\delta \approx 500\sqrt{\frac{\rho}{f}} \quad (4)$$

where the skin-depth (δ) is given in kilometres, and is approximately the depth at which the inducing field is about 30% of its surface value.

For long-period instruments, the vertical magnetic field component $B_z$ is also measured. As for the horizontal electric field, the vertical field can be also considered as a response to the Earth from source field $B_x$ and $B_y$, and is linked by the following equation:

$$\begin{pmatrix} B_z \end{pmatrix} = \begin{pmatrix} T_{xz} & T_{yz} \end{pmatrix}\begin{pmatrix} B_x \\ B_y \end{pmatrix} \quad (5)$$

The two transfer functions, $T_{xz}$ and $T_{yz}$, relate the vertical field $B_z$ to the horizontal components $B_x$ and $B_y$, respectively.

Finally, there is the problem of static shift in MT soundings (Jones, 1988). Static shift is an effect that uniformly increases or decreases the apparent resistivity responses by a constant amount. The effect is due to very near-surface changes in resistivity that locally increase or decrease the electric field. There is an analogy to static in seismic methods, and indeed the static corrections used in each case may be linked.

## Plotting of MT responses

In this paper, MT responses are plotted in three ways:

Firstly, the MT responses are presented as pseudosections. These sections show the MT responses in two modes, TE and TM, with apparent resistivity and phase plotted as a function of frequency and site location. The plots are colour contoured to give an approximate distance and depth scale, with lower frequencies penetrating deeper into the section than higher frequencies. As discussed previously, TE refers to the orientation in the 2D framework in which the electric field flows perpendicular to the 2D profile line, and hence parallel to the geological strike. TM, on the other hand, refers to the case in which the induced electric field is parallel to the 2D profile line, and hence perpendicular to the geological strike. The TM mode is often noted as being most sensitive to geological variations along the profiles (Wannamaker et al., 1984).

Secondly, the vertical field transfer functions of equation 5 are presented as what are known as induction arrows (Simpson and Bahr, 2005). As the transfer functions are complex numbers, each consists of an in-phase (or real) arrow, and an out-of-phase (or imaginary) arrow. The length of the arrow represents the size of the transfer functions, and the response to changes in lateral resistivity. These induction arrows are plotted in the Parkinson convention (Parkinson, 1962), which has the simple interpretation that real arrows point towards areas of low resistivity (and away from areas of high resistivity). These arrows are therefore very useful in demonstrating lateral resistivity changes.

Finally, data is also plotted as more complex phase tensors, which are also colour filled to indicate the primary electrical resistivity structure. For a detailed explanation of phase tensors, see Caldwell et al. (2004). The most important aspects of phase tensors are that they plot as circles for relatively uniform regions of resistivity, and are highly polarized as ellipses in more complex geology where there is a definite strike orientation in resistivity. The ellipses themselves have a 90° ambiguity, with either the major axis or the minor axis aligned with strike, depending on the geology.

## Survey and data

In Appendix 1, the tables list the locations, elevations, and lines for both long-period and broadband MT sites.

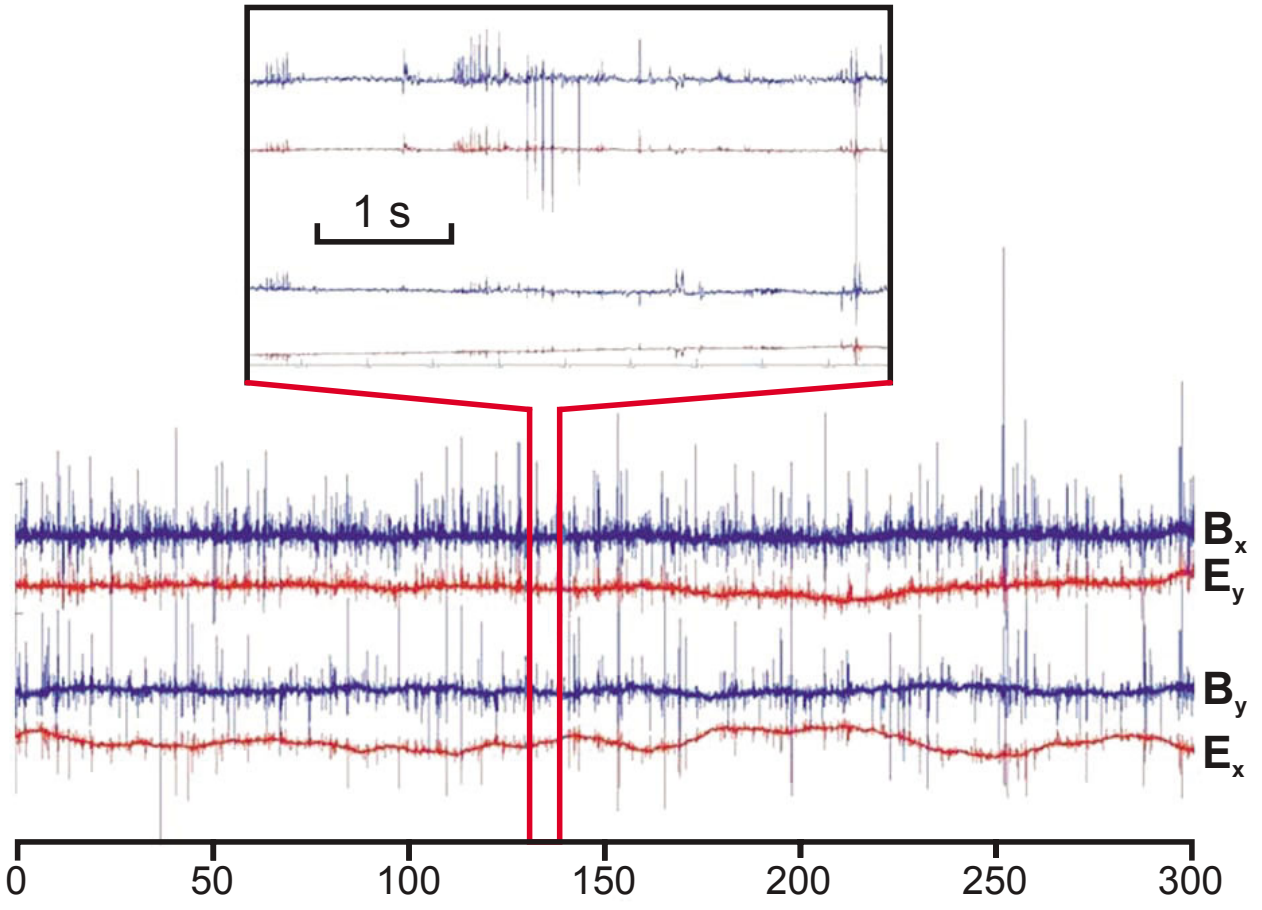


**Figure 3. Typical MT time-series data for the four horizontal components of magnetic ($B_x$, $B_y$) and electric ($E_x$, $E_y$) fields. The lower figure covers 300 s of data, sampled at 1000 Hz. The inset figure is 5 s of the same dataset, illustrating the correlation between pairs of fields.**

Typically, broadband sites were occupied for 2–3 days, and the long-period sites for 5–6 days. The figures in the Appendix indicate the duration of deployments.

Overall, instrumentation recorded high-quality time-series data. The time series were Fourier transformed to the frequency domain, and the impedance tensor [Z] (equation 1) and vertical field transfer function [T] (equation 5) determined at a wide range of frequencies. In turn, equation (1) was derived from the apparent resistivity and phases.

Processing was undertaken using the method of Chave et al. (1987), finally producing MT responses in the industry-standard Electronic Data Interchange (EDI) format.

## Modelling and inversion

Modelling and inversion of data was undertaken using the commercial WinGLink package, which incorporates the 2D inversion code of Rodi and Mackie (2001). For each model shown, the primary parameters used in the inversion are listed in the figure caption. The models are all smooth or with minimum structure, and the philosophy is one of simplicity, in presenting the least complex resistivity structures compatible with the observed MT responses.

In the following three sections, the main attributes of the three lines are outlined in terms of their data plots and the best-fitting models. In the Discussion section, the models are assessed in terms of the principal objectives of the seismic survey. However, the model sections should all be considered works in progress, and are still being refined.

## Line 10GA–CP1

Line 10GA–CP1 (approximately 150 km long) consists of 13 long-period and 39 broadband MT sites (Fig. 4). Data quality is good for all MT sites.

Figure 5 shows a plot of phase tensors for periods of 1 s and 10 s along this line. In crustal material of resistivity of 100 Ωm, the skin-depth is about 5 km for 1 s, and 15 km for 10 s. The ellipses, particularly at 10 s, are highly aligned with the geological strike in the southernmost section, but are more complex and variable in the north.

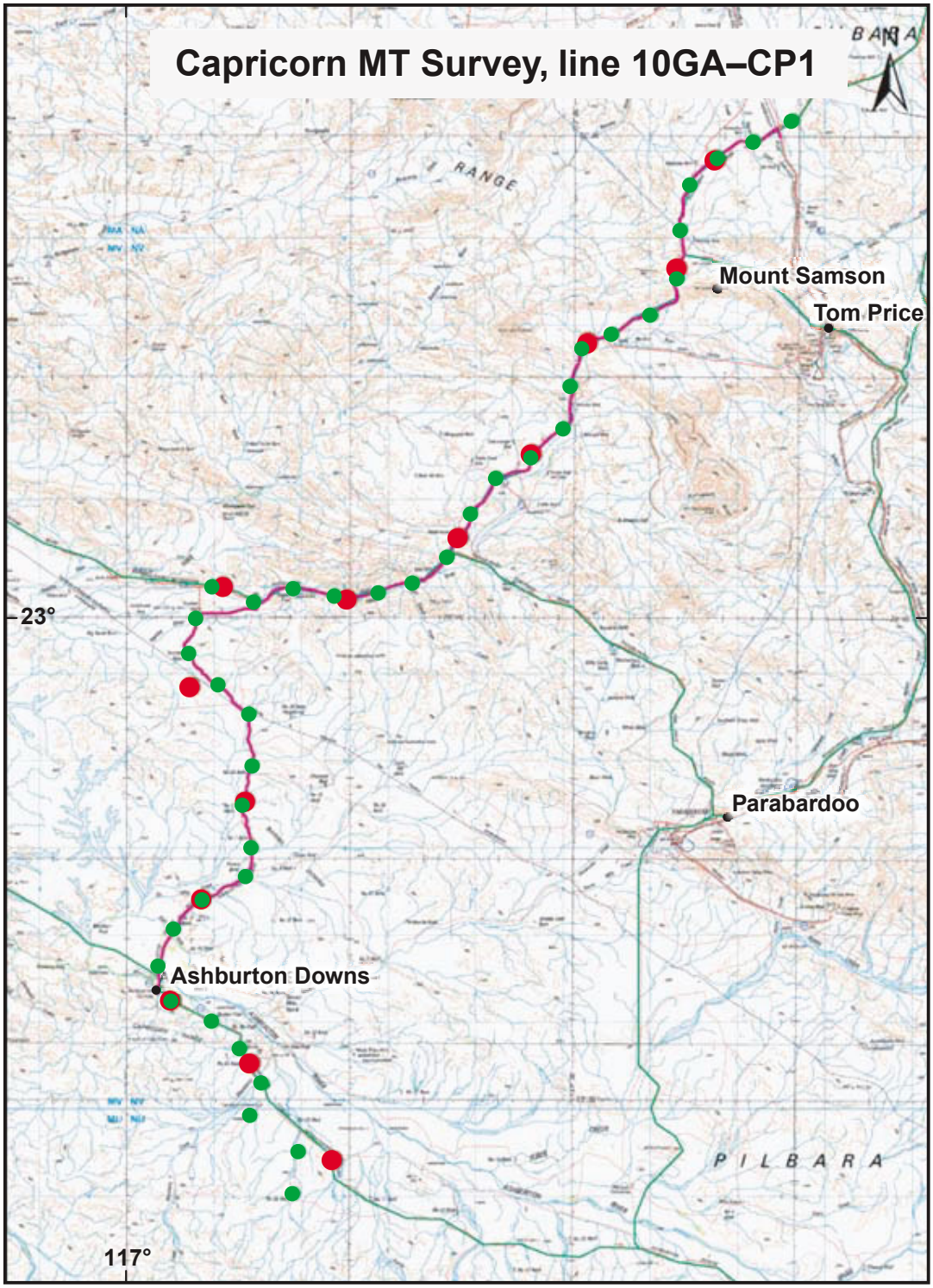


**Figure 4.** **Location of MT sites along the 10GA–CP1 profile. Broadband sites are shown in green, and are approximately 5 km apart; long-period MT sites are shown in red, and are 15 km apart. Appendix 1 lists the duration of the measurement at each site.**

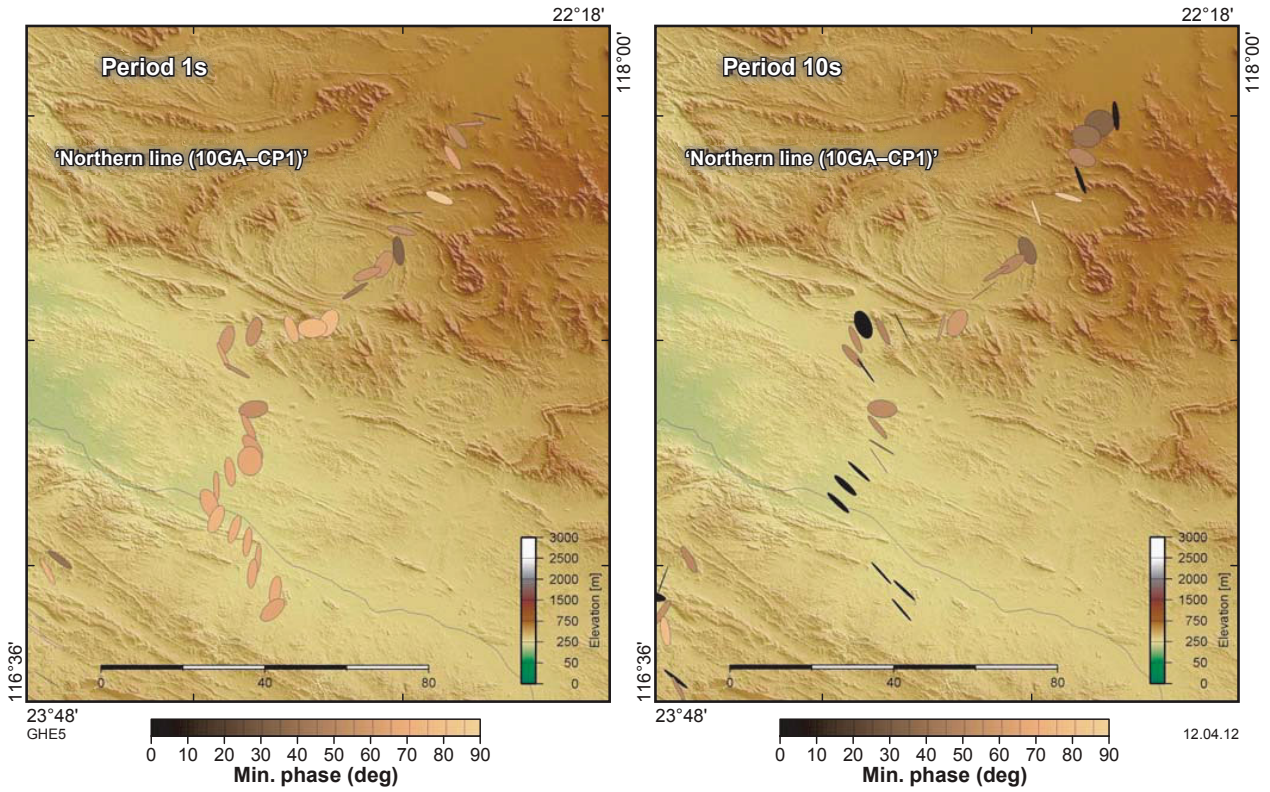


**Figure 5. Phase tensors for line 10GA–CP1 for periods of 1 s and 10 s. Ellipses are aligned with geological strike, but note there is a 90° ambiguity in terms of the alignment with the major or minor axes. For crustal materials of resistivity 100 Ωm, the skin-depths are 5 km and 15 km, respectively. The minimum phase angles are indicative of primary electrical structure: high phases (>45°) indicate high resistivity over a much lower resistivity.**

Despite this, the dominant feature of all these responses is that they are anisotropic and highly distorted.

Over longer periods, induction arrows indicate regional-scale MT responses. The vertical magnetic field was not recorded for broadband sites, so only the long-period sites, spaced 15 km apart, have induction arrows. Figure 6 shows the induction arrows for all three MT lines, for periods of 50 s, 500 s, and 5000 s. Again, for crustal material of resistivity of 100 Ωm, the skin-depths are 35 km, 110 km, and 350 km, respectively; such scale lengths can be considered in terms of the induction-scales vertically and horizontally. In other words, induction arrows at 50 s are sensitive to lateral changes in resistivity in the vicinity of 35 km away.

Note that on line 10GA–CP1 and along much of 10GA–CP2, the real arrows (red) at short periods are quite scattered (Fig. 6); however, along 10GA–CP3 the real arrows are much more uniform. At longer periods, there is a more regional trend for arrows to point to the northwest, presumably towards the deeper sediments of the Carnarvon Basin. A similar trend was noted by Selway et al. (2009) for the sites shown in Figure 1.

The broadband MT responses were inverted for 2D structure using the smooth model algorithm of Rodi and Mackie (2001). Responses were found to be approximately 2D and aligned with the strike of the geology and magnetic structures, but were quite 3D over some bandwidths. Additionally, there is evidence of significant static shift effects.

Figure 7 shows the 2D resistivity model that best fits the MT data from a bandwidth of 200 Hz – 0.1 Hz (10 s). The 39 broadband sites were carefully edited to remove bandwidths with obvious 3D effects. Inversions were run for a tau value of 0.1, with weighting on horizontal structure (alpha = 1.3) and 5% error bars. Static shifts were determined as part of the inversion, and the final model had a model misfit of about rms = 4. Figure 8 shows a pseudosection of the best-fits to the TM (with the electric field parallel to the line of the model) modes, in terms of both apparent resistivity and phase.

The most remarkable aspects of this model is that the resistivity structures are relatively uniform, and generally consists of a thin-conductive sedimentary layer at the top, then a very resistive layer (10 000 Ωm) of 2–10 km thickness, and finally a remarkably conductive (~1 Ωm) region (Fig. 7). In the model section, the structure below this conductive later is essentially unresolved, as the induced electric current do not flow any deeper; i.e. the conductive layer shields the deeper inductive response. Note too that many of the responses show evidence of 3D and possibly anisotropic conduction, which cannot be

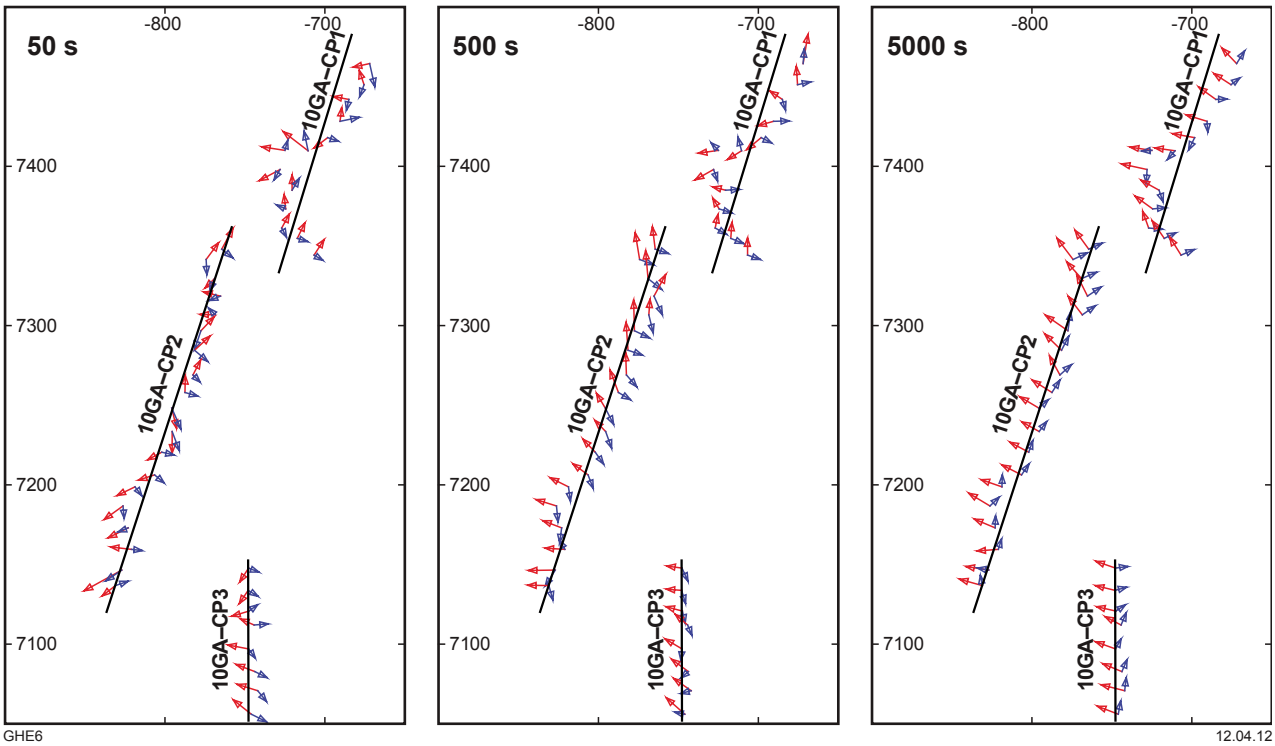


**Figure 6.** **Induction arrows at periods of 50 s, 500 s, and 5000 s for all three MT lines. The red arrows represent the in-phase (or real) component, whereas the blue arrows represent the out-of-phase (or imaginary) components. Both sets of arrows are plotted in the Parkinson convention, such that the real arrows point towards good conductors. The typical arrow size is quite small, with a magnitude of about 0.2.**

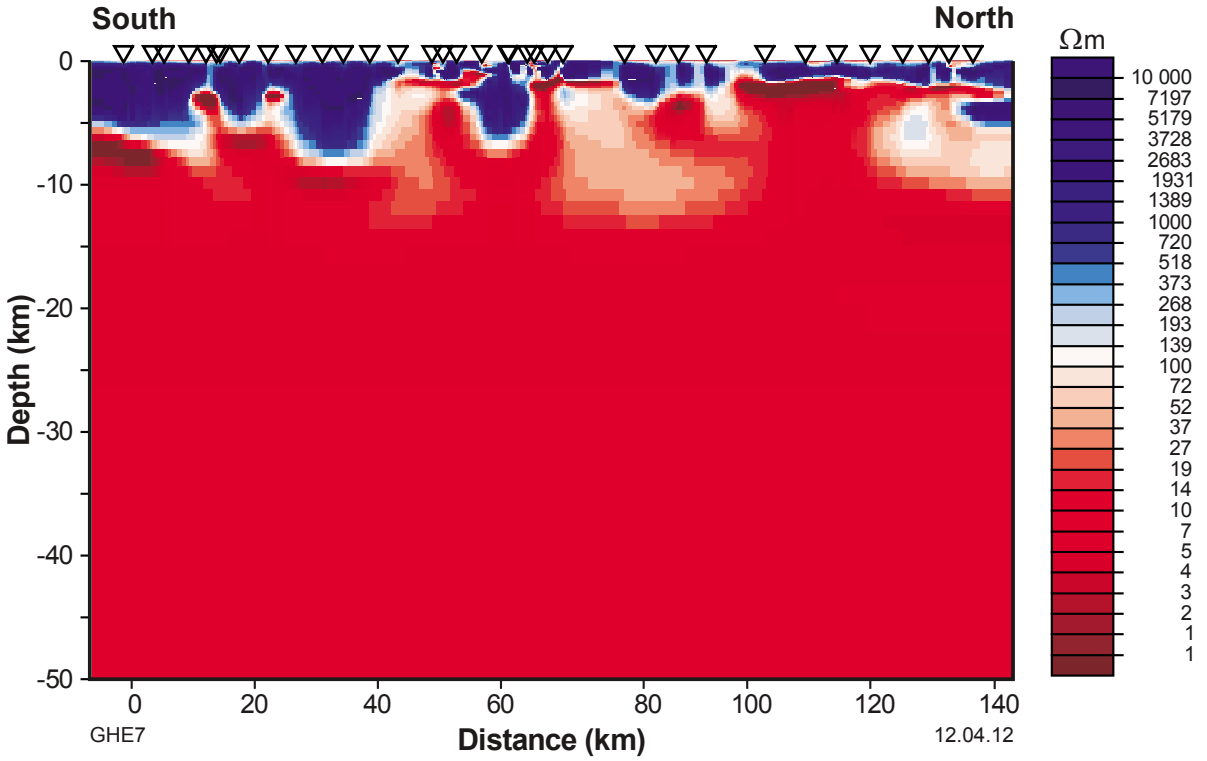


**Figure 7.** **2D resistivity section for line 10GA–CP1. The bandwidth of the inversion was 200 – 0.1 Hz, and the profile orientation was taken as being 30°E of geographic north (with geological strike perpendicular to the profile). The inversion achieved a misfit of about rms = 4 to both TE and TM mode data, with 5% errors and static shift as another model variable.**

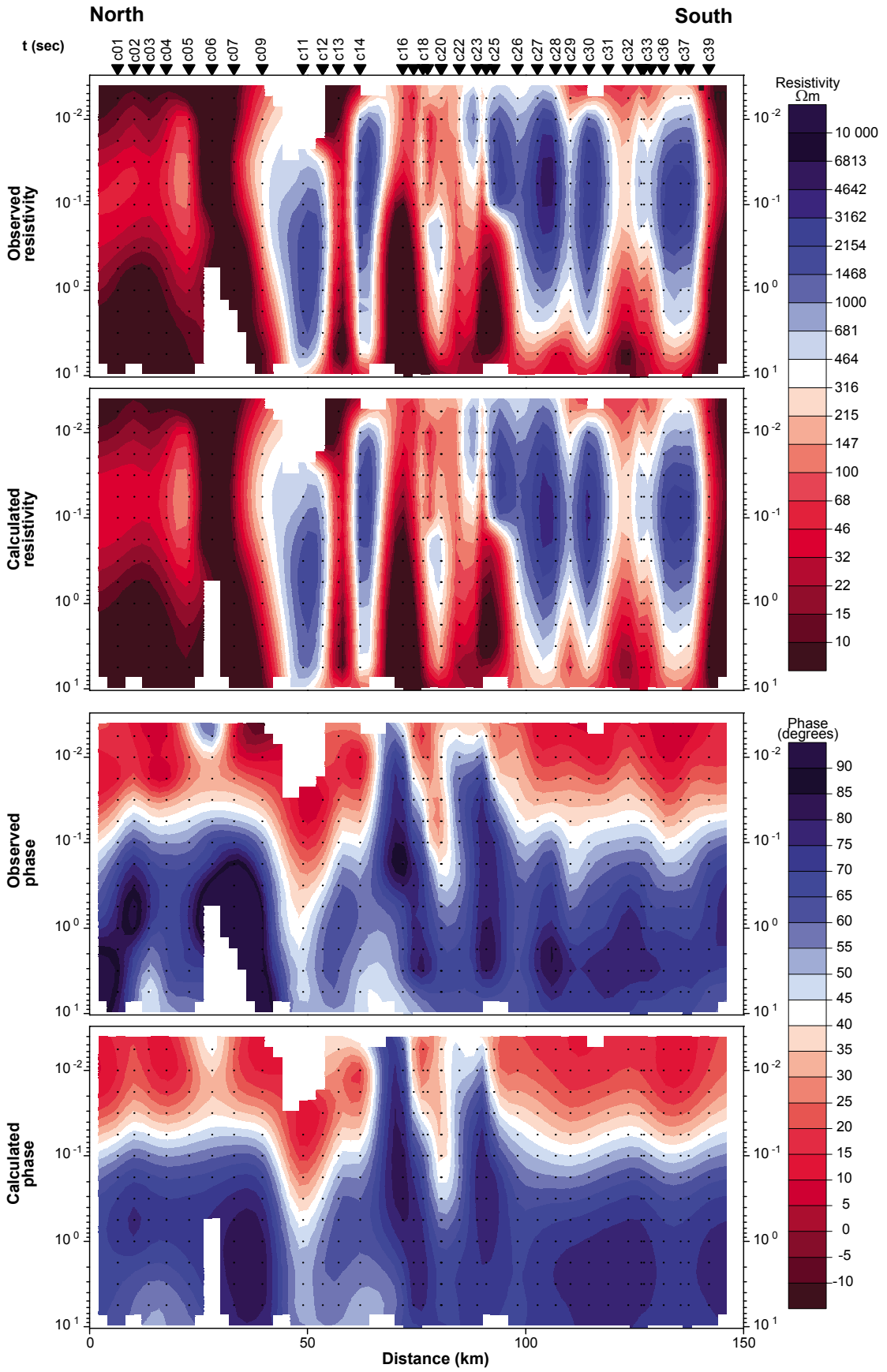


**Figure 8.** **Pseudosections for line 10GA–CP1 for the bandwidth 200 – 0.1 Hz. The top figure shows the observed TM mode apparent resistivity, and the second panel shows the calculated TM mode apparent resistivity for the model in Figure 7. Similarly, the bottom two figures show the observed and calculated phases.**

modelled with this 2D inversion approach. The southernmost section of this model shows a thicker resistive layer; this is consistent with the phase tensors seen in Figure 5, and which illustrate a change in characteristics at this point.

Long-period MT data were not modelled as the responses were generally of low quality at periods greater than 100 s and, moreover, were highly 3D. Interpretation of the low-quality responses at these long periods is made in terms of very small electric fields as the highly conducting layer effectively shorts out the induced electric currents.

## Line 10GA–CP2

Line 10GA–CP2 was the longest section (approximately 250 km), with 19 long-period and 55 broadband MT sites deployed (Fig. 9).

Figure 10 shows a plot of phase tensors along this region for periods of 1 s and 10 s. There is a remarkable change in the phase tensor characteristics about halfway along the line. To the north, phase tensors are complex, but generally highly polarized. To the south, the phase tensors are generally more circular, which indicates lower order dimensionality. However, even in the southern section, there are elliptical phase tensors, particularly at longer periods in the south.

The characteristics of the induction arrows can be seen to change with increasing period (Fig. 6). At short periods, the arrows are quite scattered along the line, suggesting heterogeneity of electrical resistivity at a scale-length smaller than the survey. At longer periods, the real arrows all align to the northwest.

As for line 10GA–CP1, the broadband MT responses were inverted for 2D structure. Responses were found to have various amounts of static shift, were approximately 2D at frequencies higher than 0.1 Hz, and were aligned with the strike of both the geological and magnetic structures. However, at quite a few sites, some bandwidths were quite 3D. Figure 11 shows the best model obtained from an inversion of MT data in the bandwidth of 200 – 0.1 Hz (10 s). The 55 broadband sites were carefully edited to remove bandwidths with obvious 3D effects. As for Figure 7, inversions were run for a tau value of 0.1, with weighting on horizontal structure and 5% error bars. Static shifts were determined as part of the inversion, and the final model obtained a model misfit of about rms = 4. Figure 12 shows pseudosections of the best-fits to the observed TM (with the electric field parallel to the line of the model) modes, in terms of both apparent resistivity and phase.

The most remarkable aspects of this model is that the resistivity structure of the northern section is similar to the entirety of 10GA–CP1 (Fig. 11). In most parts, it consists of a thin-conductive sedimentary layer, followed by a very resistive layer (10 000 Ωm) 2–10 km thick, and finally a remarkably conductive (~1 Ωm) region at the base. In the model section, the structure below this conductive later is unresolved, as the induced electric current does not flow any deeper; i.e. the conductive layer shields the deeper responses. Many of the responses also show evidence of 3D and possibly anisotropic conduction that cannot be modelled with this 2D inversion approach.

However, in the southern part of 10GA–CP2, the crustal resistivity section shows a profound change where the phase tensors become more uniform (Fig. 10). The distinct electrical contrast between the Bandee Seismic Province and the Glenburgh Terrane dips at about the same angle as the Lyons River Fault, which is interpreted to be the suture zone between the Pilbara Craton and Glenburgh Terrane. Although there is evidence of conductive shear zones (which are coincident with some of the more polarized phase tensors in Figure 10), which may be related to the Ti Tree Shear Zone, the bulk of the crust is resistive (>1000 Ωm), which is considered more typical of Archean crustal profiles. The Minnie Creek batholith (as shown in Figure 1a and Frontispiece 1) was not resolved as a separate body, but its southern margin is coincident with a profound change in the crustal resistivity across the Lyons River Fault.

Again, long-period data was unable to modelled, due to the fact that data from sites in the north were of very low quality, and were 3D.

## Line 10GA–CP3

Line 10GA–CP3 was the shortest (approximately 100 km), with eight long-period and 22 broadband MT sites deployed (Fig. 13).

Figure 14 shows a plot of phase tensors along this line for periods of 1 s and 10 s. These phase tensors are relatively uniform, with the only change occurring at the seventh site along the line, which indicates a more 2D structure. Interestingly, this site coincides approximately with the Errabiddy Shear Zone.

In Figure 6, the long-period induction arrows can be seen to be relatively uniform, but show a slight convergence to the north, indicating a conductive flow of current roughly aligned with the Errabiddy Shear Zone.

Broadband MT responses were again inverted for 2D structure (Fig. 15) using the same modelling parameters as for 10GA–CP1 (Fig. 7) and 10GA–CP2 (Fig. 11). Pseudosection fits are also shown for the TM mode in Figure 16. Overall, the MT responses are relatively simple, with the exception of the site directly on the shear zone, which exhibits a response indicating the strong channelling of electric currents.

The model section seen in Figure 15 is relatively simple and resistive (~1000 Ωm), but shows evidence of a conductive shear zone aligned with the Errabiddy Shear Zone. In this section, the shear zone does not fully intersect the surface, but coincides with a relatively broad (~10 km) region of low resistivity. The depth extent for this body is not clear from the modelling; although it appears to disappear at a depth of about 25 km, this is also about the skin-depth and from the broadband data the depth extent is unresolved. For most of the line, the resistive sections are imaged much deeper, as the skin-depths are much greater.

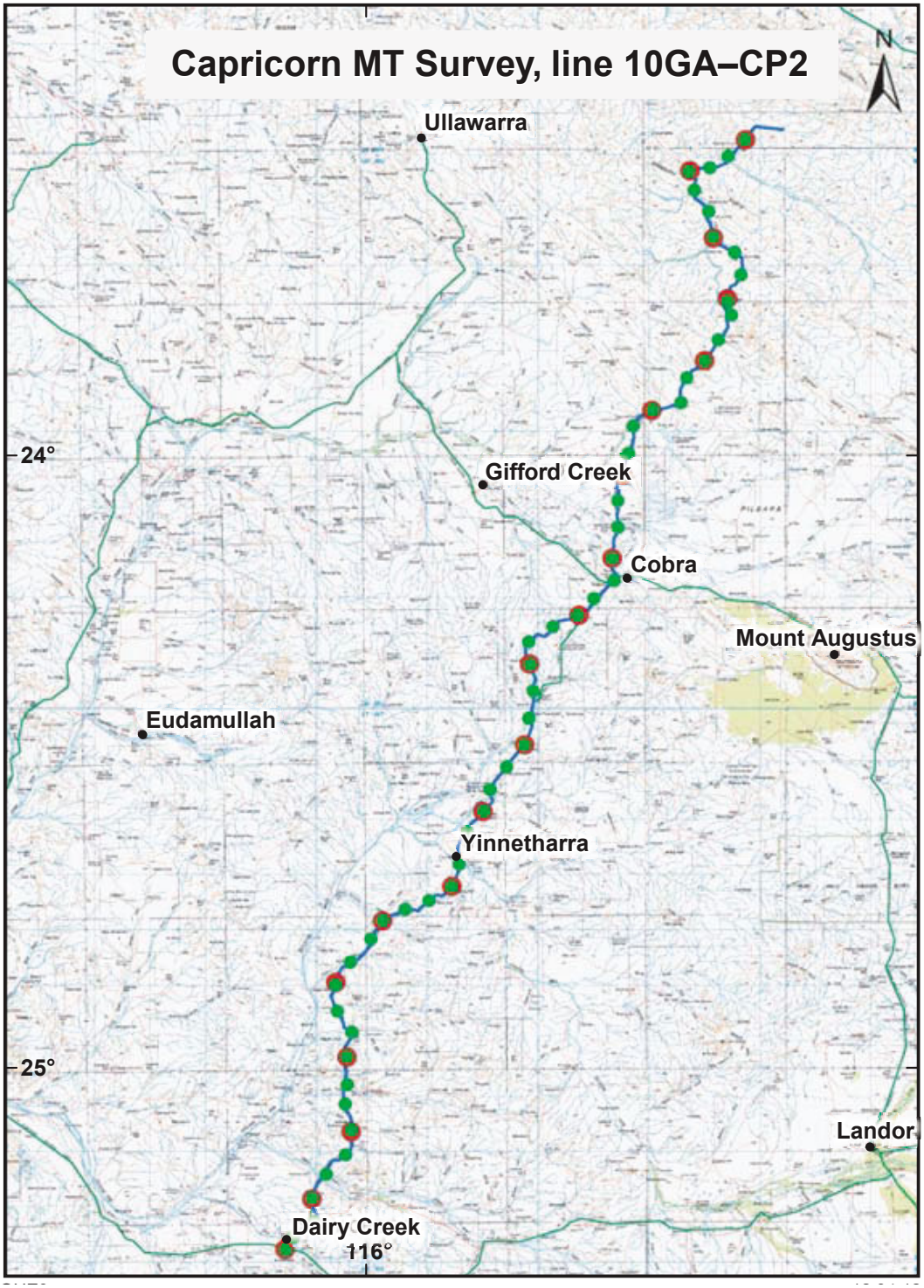


**Figure 9.** **Location of MT sites along the 10GA–CP2 profile. Broadband sites are shown in green, and are approximately 5 km apart; long-period MT sites are shown in red, and are 15 km apart. Appendix 1 lists the duration of the measurement at each site.**

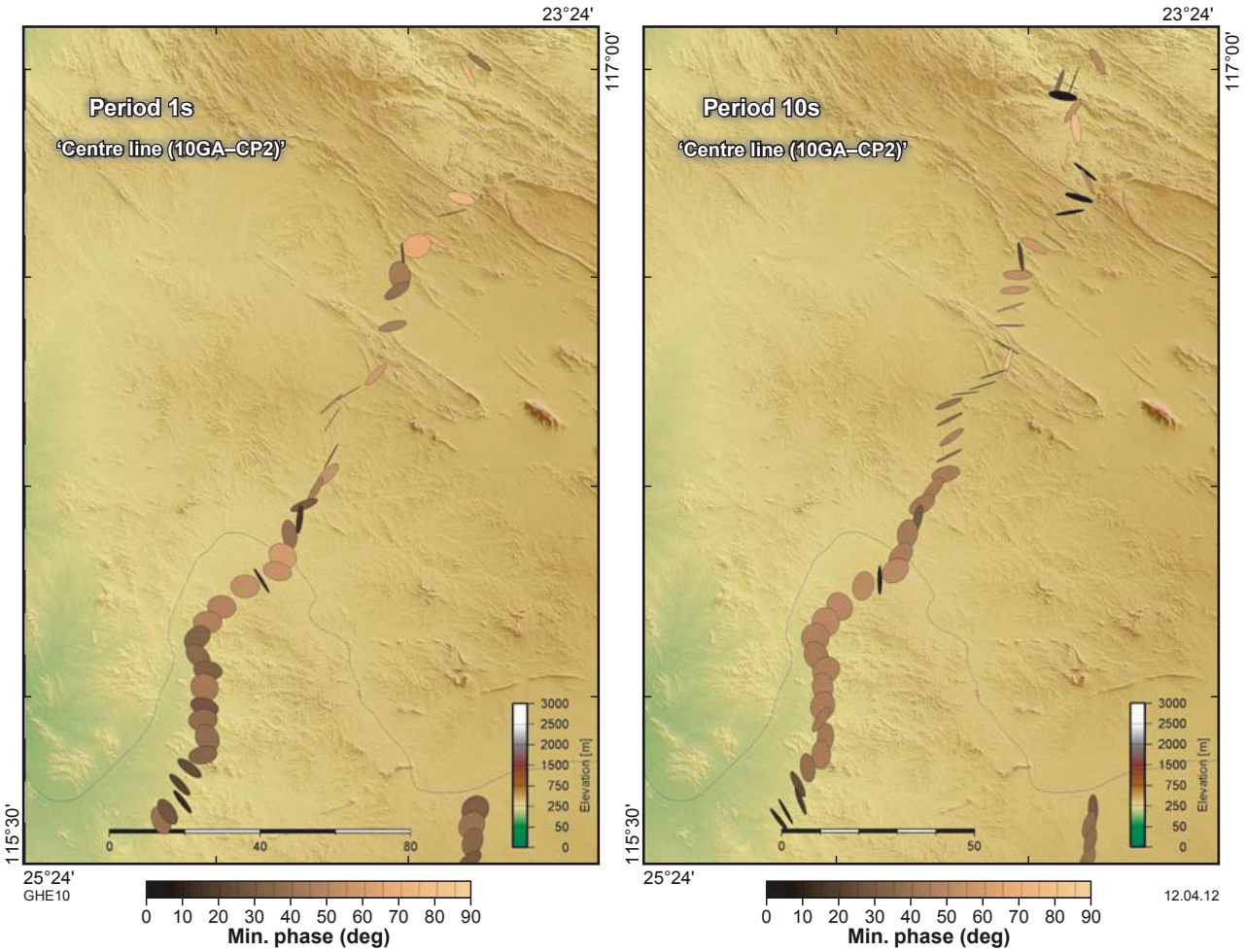


**Figure 10. Phase tensors for line 10GA–CP2 for periods of 1 s and 10 s. Ellipses are aligned with geological strike, but note there is a 90° ambiguity in terms of the alignment with the major or minor axes. For crustal materials of resistivity 100 Ωm, the skin-depths are 5 km and 15 km, respectively. The minimum phase angles are indicative of primary electrical structure: high phases (>45°) indicate high resistivity over a much lower resistivity.**

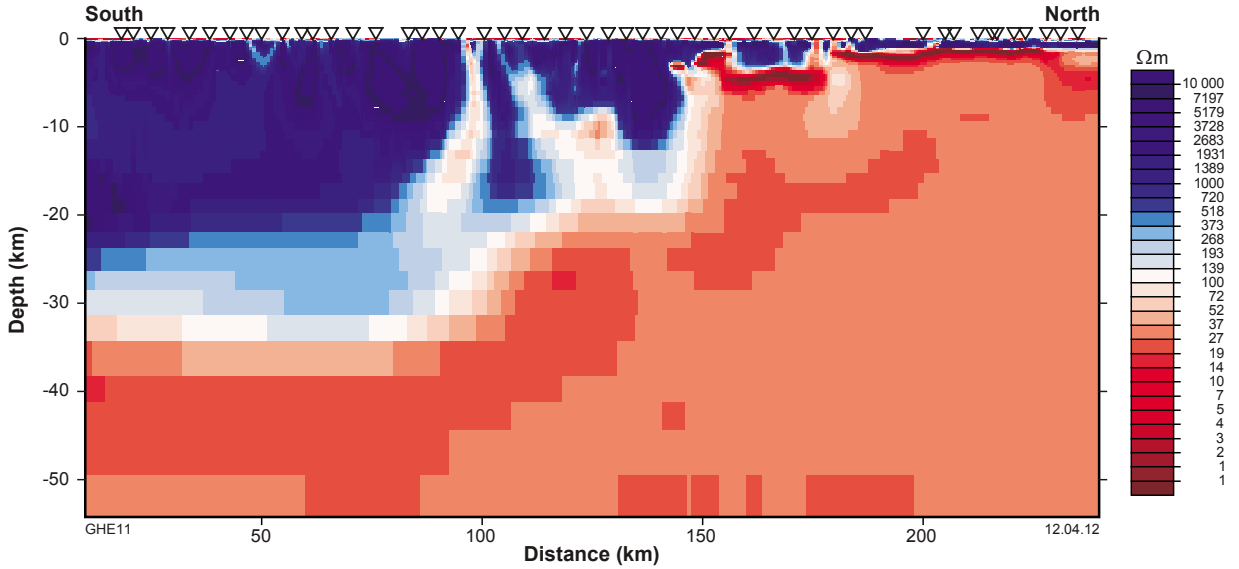


**Figure 11. 2D resistivity section for line 10GA–CP2. The bandwidth of the inversion was 200 – 0.1 Hz, and the profile orientation was taken as being 30°E of geographic north (with geological strike perpendicular to the profile). The inversion achieved a misfit of about rms = 4 to both TE and TM mode data, with 5% errors and static shift as another model variable.**

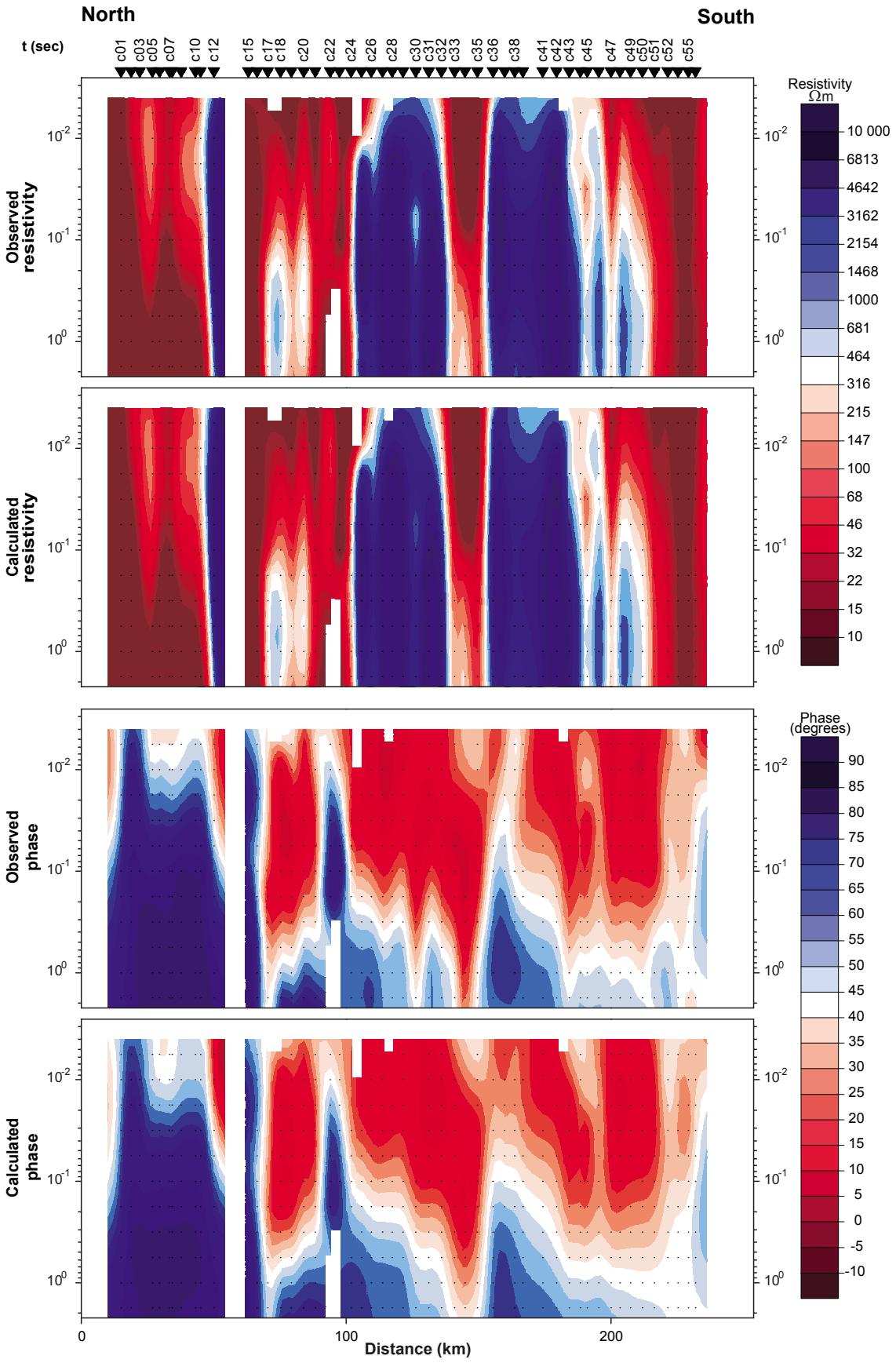


**Figure 12. Pseudosections for line 10GA–CP2 for the bandwidth 200 – 0.1 Hz. The top figure shows the observed TM mode apparent resistivity, and the second panel shows the calculated TM mode apparent resistivity for the model in Figure 11. Similarly, the bottom two figures show the observed and calculated phases.**

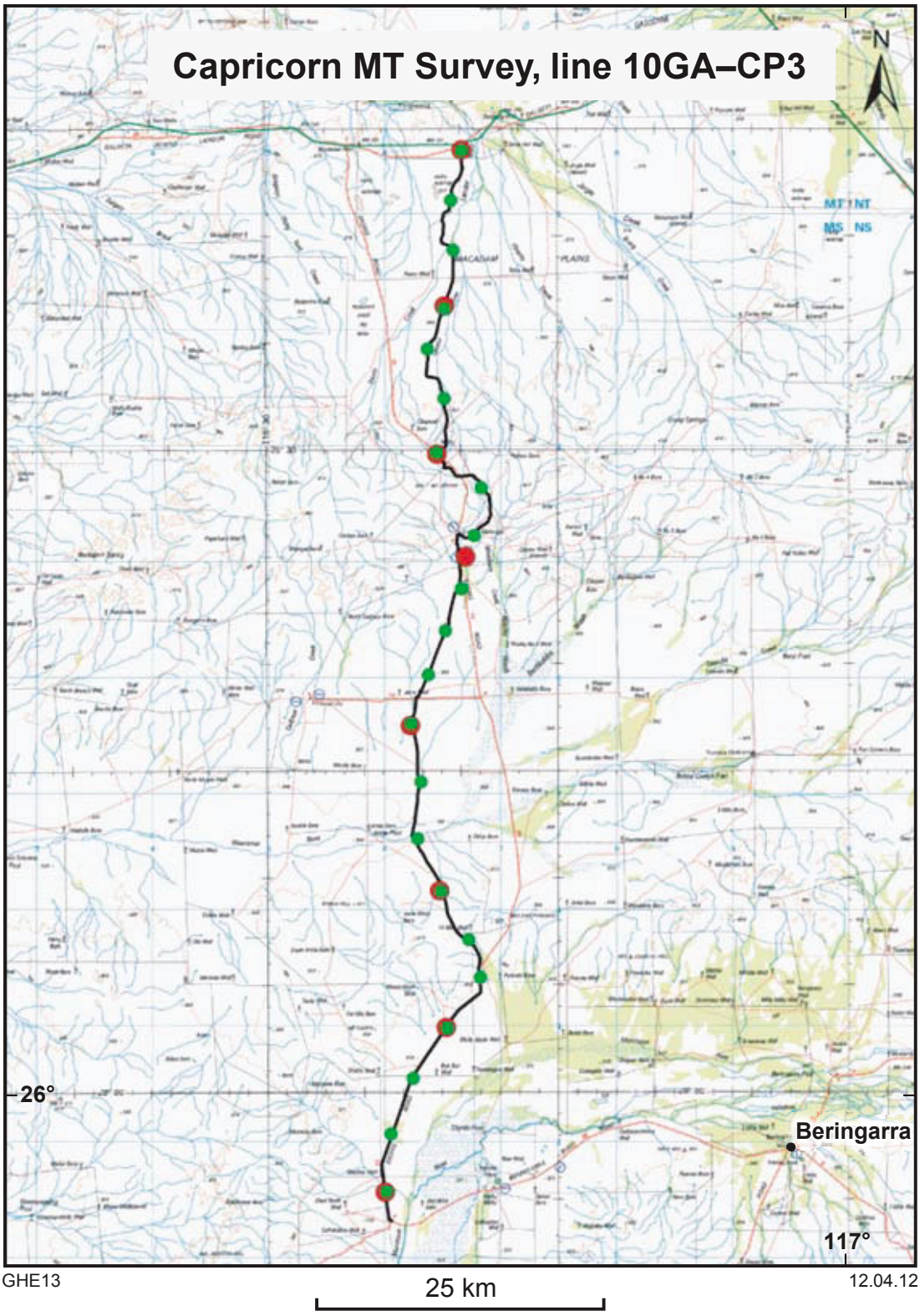


**Figure 13. Location of MT sites along the 10GA–CP3 profile. Broadband sites are shown in green, and are approximately 5 km apart; long-period MT sites are shown in red, and are 15 km apart. Appendix 1 lists the duration of the measurement at each site.**

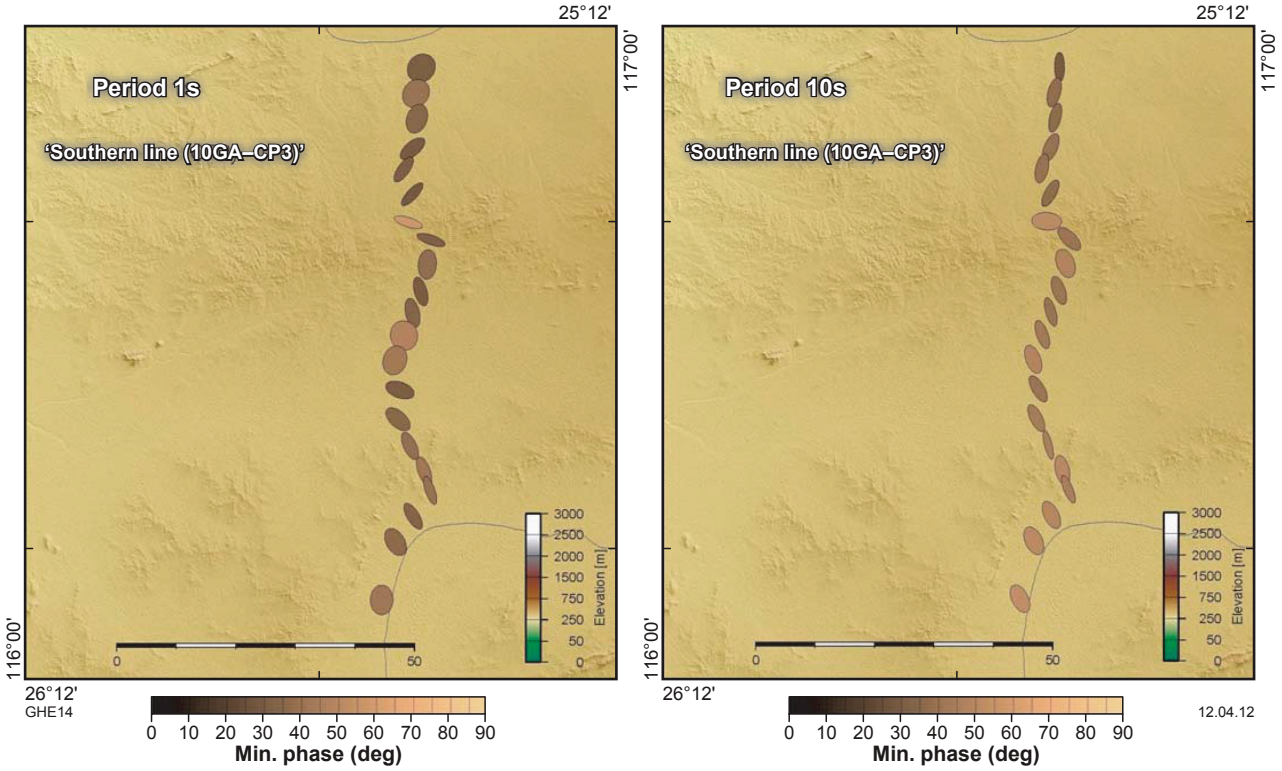


**Figure 14: Phase tensors for line 10GA–CP3 for periods of 1 s and 10 s. Ellipses are aligned with geological strike, but note there is a 90° ambiguity in terms of the alignment with the major or minor axes. For crustal materials of resistivity 100 Ωm, the skin-depths are 5 km and 15 km, respectively. The minimum phase angles are indicative of primary electrical structure: low phases (<45°) indicate low resistivity over a much higher resistivity.**

Long-period MT sites were also inverted. Only in this line section were long-period MT responses of high enough quality to a period of 10 000 s. Only seven of the eight long-period sites were modelled (Fig. 17), as the response at the site on the shear zone was very anisotropic. The most remarkable aspect of this model is that the low-resistivity region is imaged much deeper, and appears to dip towards the south when compared to the models for the other lines (Fig. 17).

## Discussion and conclusion

Modelling is not complete, as the results from Selway et al. (2009) will be added to complement the current observations and there will be an attempt to improve the MT response estimation through the application of a number of processing refinements. However, it is unlikely that any new model will significantly differ from those presented here (Figs 7, 11, 15, and 17).

Figure 18 shows a composite model and a preliminary interpretation of the uppermost 25 km along the Capricorn study line, with the three profiles linked together. Figure 19 shows a composite model, for line 10GA–CP3 only, incorporating both the broadband and long-period MT sites to a depth of 200 km. Here, the outcomes are listed in terms of the primary seismic objectives.

1. The Errabiddy Shear Zone is clearly indentified in section 10GA–CP3 (Fig. 18), and appears as a zone of low resistivity, approximately 10 km wide, and extending to at least 25 km depth. The Shear Zone appears to be near-vertical, and exhibits some more complex geometry near the surface (Fig. 18). To examine the deep structure, a comparison, for line 10GA–CP3 only, of both the broadband and long-period MT sites to a depth of 200 km was made (Fig. 19). Although the long-period MT sites lack the resolution at depths of 50 km and more, there is an overall trend of a south-dipping structure evident in both the low-resistivity shear zone, and in the more resistive structures to the south.

2. The depth and geometry of the Minnie Creek batholith was not resolved, but it is noted that the location of this batholith is coincident with a profound change in the crustal resistivity along line 10GA–CP2, which in turn appears to be coincident with the Lyons River Fault.

3. The models resolve very little in terms of basin structure and faults in the Pilbara–Hamersley–Ashburton line, 10GA–CP1. This is primarily due to the low-resistivity structures observed at depths of 2–10 km. Thus, there is little quantitative information at present for the other objectives defined

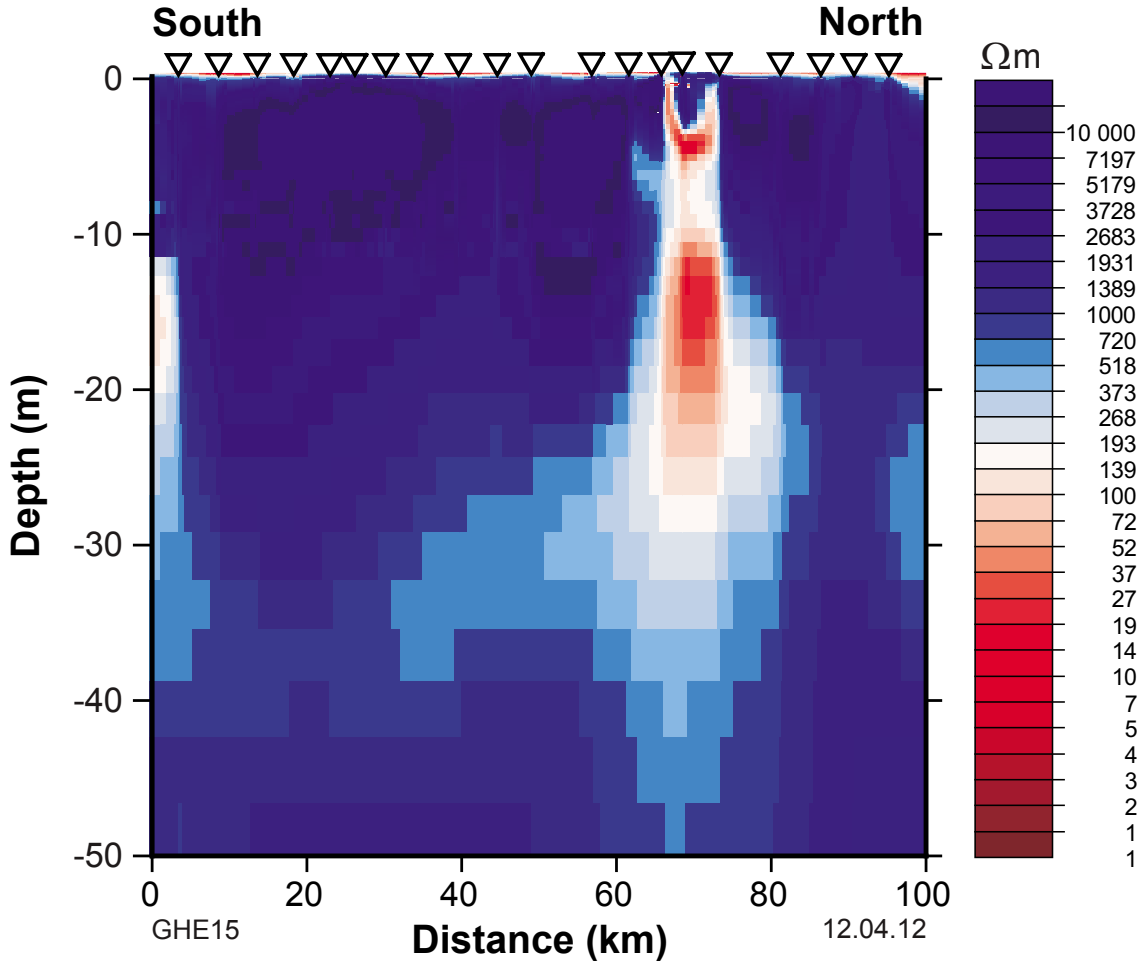


**Figure 15. 2D resistivity section for line 10GA–CP3. The bandwidth of the inversion was 200 – 0.1 Hz, and the profile orientation was taken as being geographic north (with geological strike perpendicular to the profile). The inversion achieved a misfit of about rms = 4 to both TE and TM mode data, with 5% errors and static shift as another model variable.**

for the Capricorn Seismic study, although a closer comparison with the interpreted seismic section may yield important new constraints on these structures.

## Acknowledgement

We acknowledge the Western Australian Government's Exploration Incentive Scheme (EIS) and the Australia Federal Government's National Earth Science Infrastructure Program (AuScope) for funding of the MT program; and GSWA and Geoscience Australia are thanked for providing significant logistical support for fieldwork. The authors gratefully acknowledge the pastoralists and Aboriginal communities from the survey region for allowing us land access. We are indebted to the many station owners along this profile that provided accommodation for the field crews, and thereby made the survey achievable. The University of Adelaide is thanked for the ongoing technical, administrative, and research support that makes this, and other surveys, feasible.

## References

Caldwell, TG, Bibby, HM and Brown, C 2004, The magnetotelluric phase tensor: Geophysical Journal International, v. 158, no. 2, p. 457–469.

Chave, AD, Thompson, DJ and Ander, ME 1987, On the robust estimation of power spectra, coherences and transfer functions: Journal of Geophysical Research — Solid Earth, v. 92, p. 633–648.

Jones, AG 1988, Static shift of magnetotelluric data and its removal in a sedimentary basin environment: Geophysics, v. 53, p. 967–978.

Parkinson, WD 1962, The influence of continents and oceans on geomagnetic variations: Geophysical Journal of the Royal Astronomical Society, v. 6, p. 441–449.

Rodi, W and Mackie, RL 2001, Nonlinear conjugate gradients algorithm for 2-D magnetotelluric inversion: Geophysics, v. 66, no. 1, p. 174–187.

Selway, K, Sheppard, S, Thorne, AM, Johnson, SP and Groenewald, PB 2009, Identifying the lithospheric structure of a Precambrian orogen using magnetotellurics: The Capricorn Orogen, Western Australia: Precambrian Research, v. 168, p. 185–196.

Simpson, F and Bahr, K 2005, Practical Magnetotellurics: Cambridge University Press, Cambridge, UK, 270p.

Wannamaker, PE, Hohmann, GW and Ward, SH 1984, Magnetotelluric responses of three-dimensional bodies in layered earths: Geophysics, v. 49, p. 1517–1533.

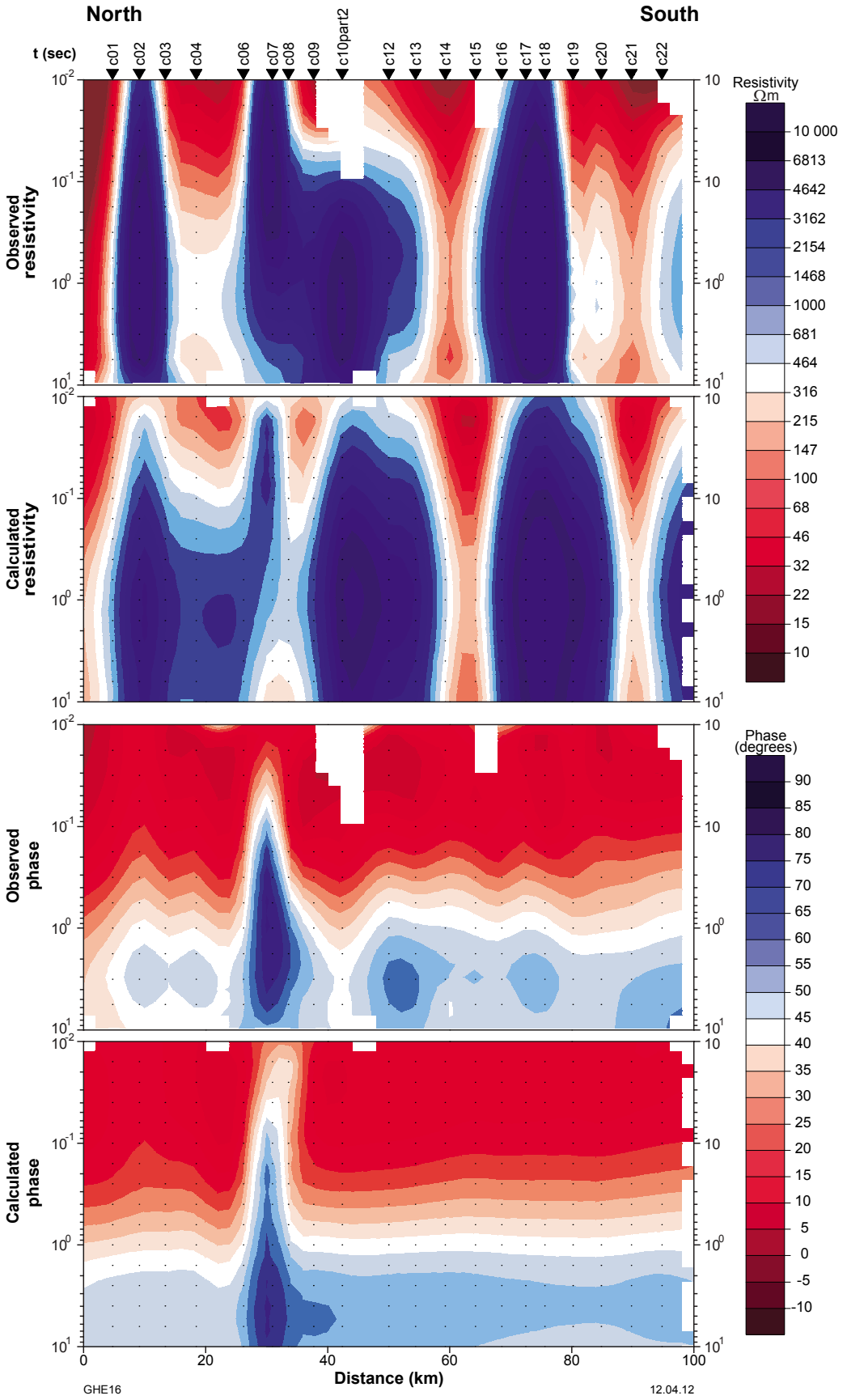


**Figure 16. Pseudosections for line 10GA–CP3 for the bandwidth 200 – 0.1 Hz. The top figure shows the observed TM mode apparent resistivity, and the second panel shows the calculated TM mode apparent resistivity for the model in Figure 15. Similarly, the bottom two figures show the observed and calculated phases.**

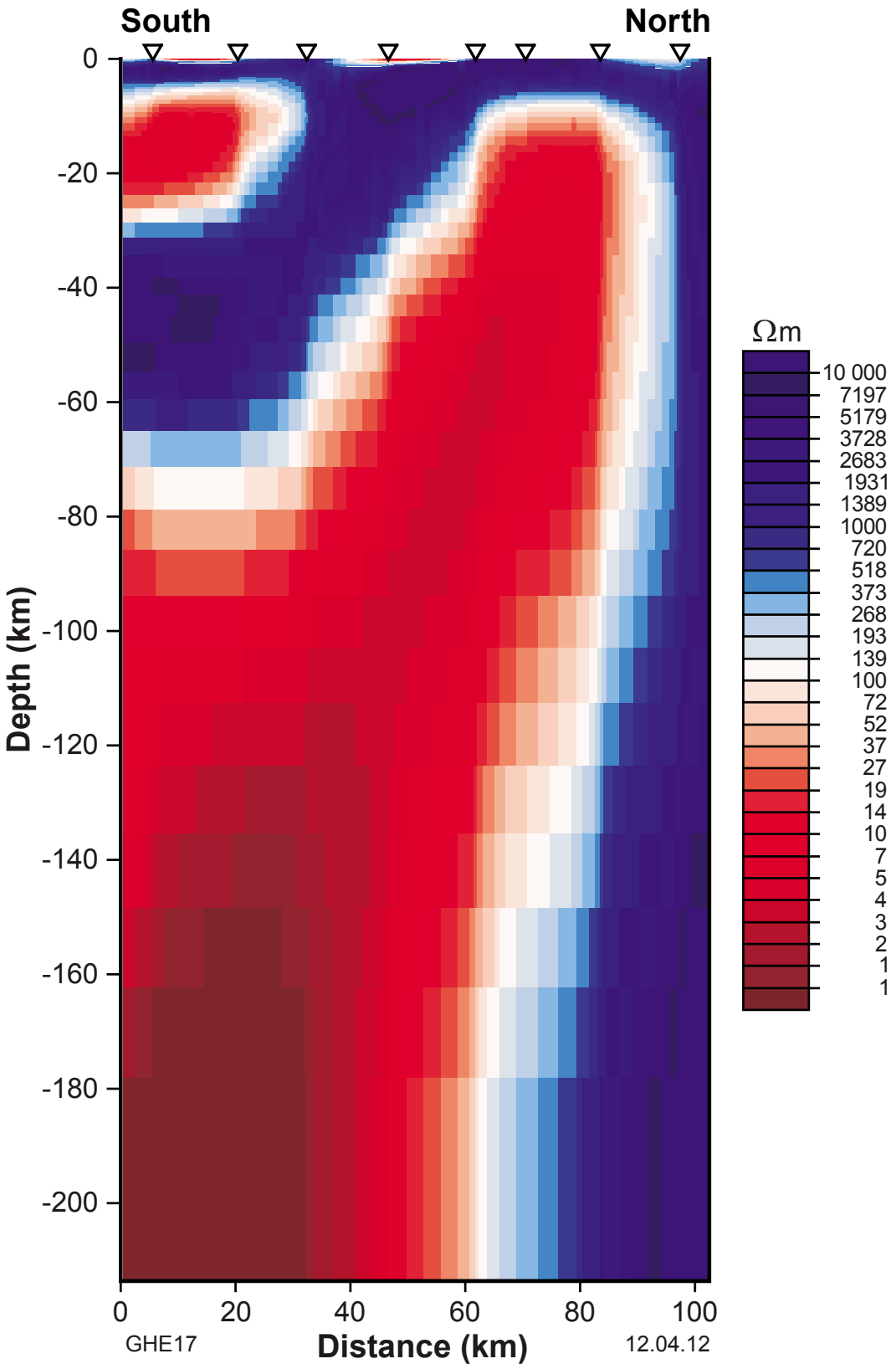


**Figure 17. Deep resistivity structure beneath line 10GA–CP3. Note that there is a change in colour scale (compared to Figures 7, 11, and 15), such that the minimum is now 100 Ωm.**

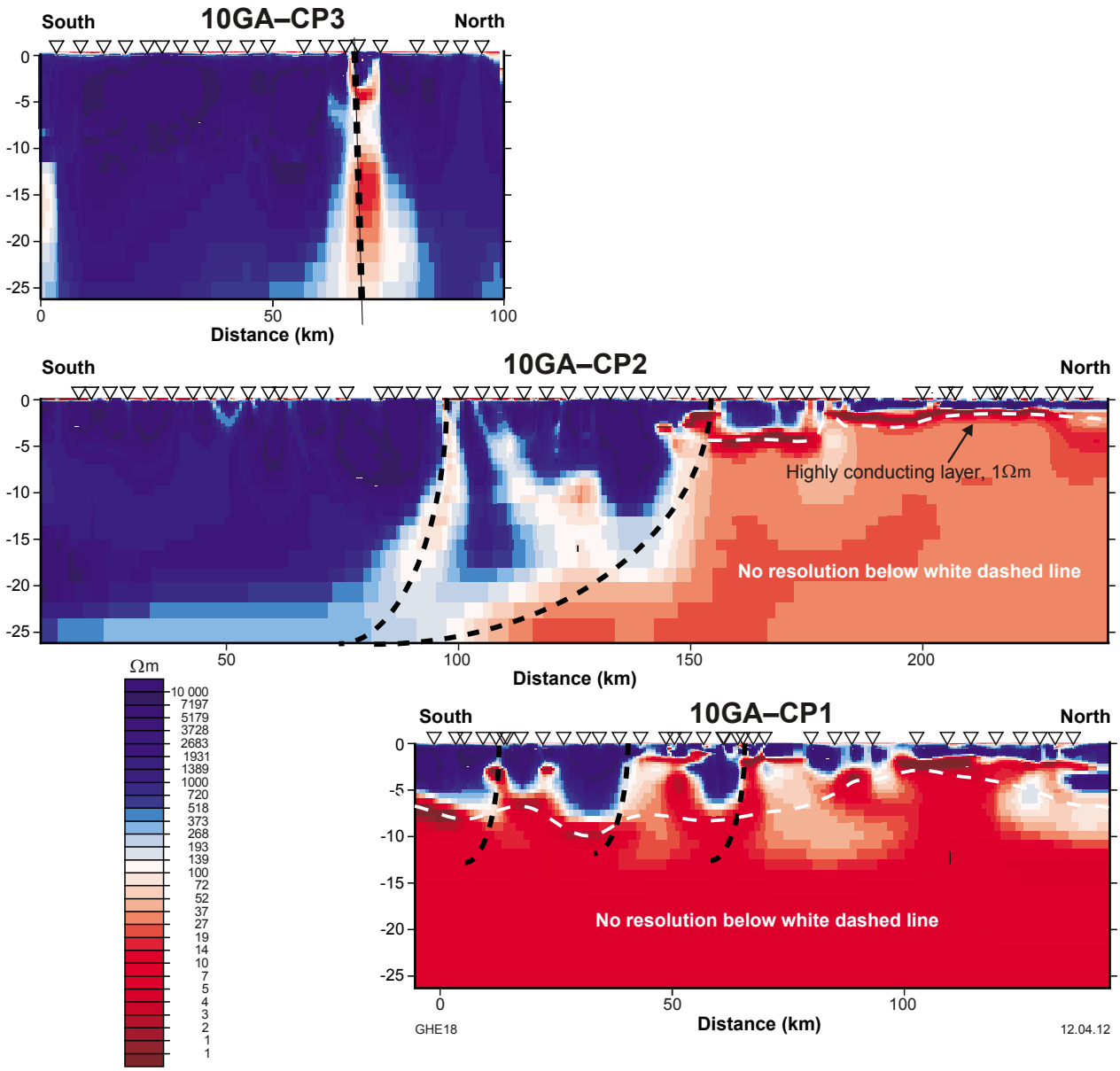


**Figure 18. Preliminary interpretation of the three MT sections to a depth of 25 km.**

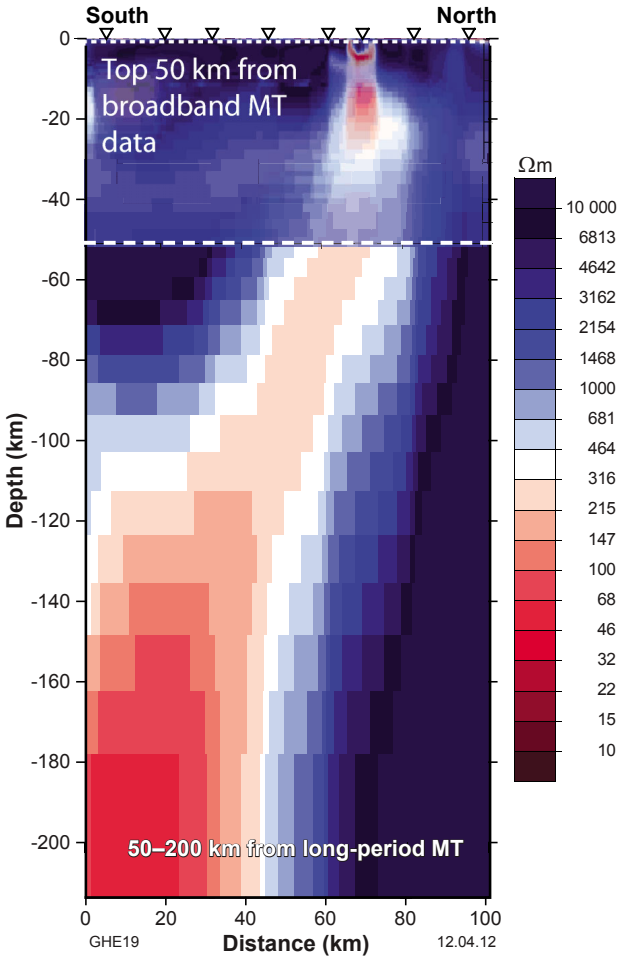


**Figure 19. Broadband (top) and long-period (bottom) models for line 10GA–CP3, both at approximately the same scale.**

# Appendix 1

| Station | Long | | Lat | | Decimal Coordinates | | | | | |
|---|---|---|---|---|---|---|---|---|---|---|
| Station | (°) | (') | (°) | (') | Long (°) Longitude_dd | Lat (°) Latitude_dd | Elevation | Easting | Northing | Zone |
| CP1B01 | 117 | 44.557 | 22 | 28.985 | 117.743 | -22.483 | 639 | 513511 | 7513511 | 50 |
| CP1B02 | 117 | 41.973 | 22 | 30.269 | 117.700 | -22.504 | 634 | 571950 | 7511164 | 50 |
| CP1B03 | 117 | 39.599 | 22 | 31.305 | 117.660 | -22.522 | 642 | 567873 | 7509270 | 50 |
| CP1B04 | 117 | 37.738 | 22 | 33.001 | 117.629 | -22.550 | 653.7 | 564672 | 7506156 | 50 |
| CP1B05 | 117 | 37.092 | 22 | 35.821 | 117.618 | -22.597 | 603.9 | 563542 | 7500957 | 50 |
| CP1B06 | 117 | 36.898 | 22 | 38.822 | 117.615 | -22.647 | 584 | 563188 | 7495421 | 50 |
| CP1B07 | 117 | 35.164 | 22 | 41.127 | 117.586 | -22.685 | 585 | 560198 | 7491177 | 50 |
| CP1B08 | 117 | 32.543 | 22 | 42.304 | 117.542 | -22.705 | 544 | 555704 | 7489029 | 50 |
| CP1B09 | 117 | 30.541 | 22 | 43.191 | 117.509 | -22.720 | 526.9 | 552267 | 7487401 | 50 |
| CP1B10 | 117 | 29.76 | 22 | 45.547 | 117.496 | -22.759 | 516.9 | 550920 | 7486061 | 50 |
| CP1B11 | 117 | 29.293 | 22 | 48.213 | 117.488 | -22.804 | 473.4 | 550107 | 7478144 | 50 |
| CP1B12 | 117 | 27.17 | 22 | 50.012 | 117.453 | -22.834 | 451 | 546463 | 7474836 | 50 |
| CP1B13 | 117 | 24.806 | 22 | 51.271 | 117.413 | -22.855 | 448 | 542415 | 7472526 | 50 |
| CP1B14 | 117 | 23.091 | 22 | 53.521 | 117.385 | -22.892 | 433 | 539471 | 7468384 | 50 |
| CP1B15 | 117 | 21.559 | 22 | 56.19 | 117.359 | -22.937 | 398.4 | 536842 | 7463465 | 50 |
| CP1B16 | 117 | 19.234 | 22 | 57.836 | 117.321 | -22.964 | 381 | 532860 | 7460438 | 50 |
| CP1B17 | 117 | 16.944 | 22 | 58.46 | 117.282 | -22.974 | 366 | 528947 | 7459294 | 50 |
| CP1B18 | 117 | 13.974 | 22 | 58.632 | 117.233 | -22.977 | 349 | 523871 | 7458986 | 50 |
| CP1B19 | 117 | 11.206 | 22 | 58.193 | 117.187 | -22.970 | 343 | 519142 | 7459802 | 50 |
| CP1B20 | 117 | 8.569 | 22 | 58.982 | 117.143 | -22.983 | 318.4 | 514639 | 7458350 | 50 |
| CP1B21 | 117 | 5.769 | 22 | 58.073 | 117.096 | -22.968 | 305.6 | 509854 | 7460033 | 50 |
| CP1B22 | 117 | 4.676 | 23 | 0.025 | 117.078 | -23.000 | 295.2 | 507986 | 7456432 | 50 |
| CP1B23 | 117 | 4.204 | 23 | 2.219 | 117.070 | -23.037 | 285 | 507179 | 7452387 | 50 |
| CP1B24 | 117 | 6.148 | 23 | 4.177 | 117.102 | -23.070 | 290 | 510495 | 7448770 | 50 |
| CP1B25 | 117 | 8.246 | 23 | 6 | 117.137 | -23.100 | 285 | 514074 | 7445411 | 50 |
| CP1B26 | 117 | 8.475 | 23 | 9.233 | 117.141 | -23.154 | 279 | 514460 | 7439440 | 50 |
| CP1B27 | 117 | 7.831 | 23 | 11.656 | 117.131 | -23.194 | 260 | 513358 | 7434967 | 50 |
| CP1B28 | 117 | 8.421 | 23 | 14.329 | 117.140 | -23.239 | 256 | 514358 | 7430037 | 50 |
| CP1B29 | 117 | 8.023 | 23 | 16.131 | 117.134 | -23.269 | 240 | 513675 | 7426713 | 50 |
| CP1B30 | 117 | 5.168 | 23 | 17.56 | 117.086 | -23.293 | 238 | 508808 | 7424079 | 50 |
| CP1B31 | 117 | 3.189 | 23 | 19.408 | 117.053 | -23.323 | 235 | 505433 | 7420671 | 50 |
| CP1B32 | 117 | 2.179 | 23 | 21.7 | 117.036 | -23.362 | 237 | 503713 | 7416442 | 50 |
| CP1B33 | 117 | 3.161 | 23 | 23.853 | 117.053 | -23.398 | 242 | 505384 | 7412470 | 50 |
| CP1B34 | 117 | 5.778 | 23 | 25.152 | 117.096 | -23.419 | 240 | 509838 | 7410071 | 50 |
| CP1B35 | 117 | 7.668 | 23 | 26.823 | 117.128 | -23.447 | 250 | 513054 | 7406985 | 50 |
| CP1B36 | 117 | 9.175 | 23 | 29.01 | 117.153 | -23.484 | 248 | 515615 | 7402946 | 50 |
| CP1B37 | 117 | 8.359 | 23 | 30.997 | 117.139 | -23.517 | 258 | 514224 | 7399279 | 50 |
| CP1B38 | 117 | 11.644 | 23 | 33.251 | 117.194 | -23.554 | 263 | 519805 | 7395118 | 50 |
| CP1B39 | 117 | 11.246 | 23 | 35.846 | 117.187 | -23.597 | 276 | 519124 | 7390329 | 50 |

| Station | Long | | Lat | | Decimal Coordinates | | | | | |
|---|---|---|---|---|---|---|---|---|---|---|
| | (°) | (') | (°) | (') | Long (°) | Lat (°) | | | | |
| Station | | | | | Longitude_dd | Latitude_dd | Elevation | Easting | Northing | Zone |
| CP2B01 | 116 | 40.803 | 23 | 29 | 116.680 | -23.486 | 339 | 467330 | 7402597 | 50 |
| CP2B02 | 116 | 39.032 | 23 | 31 | 116.651 | -23.513 | 304 | 464321 | 7399642 | 50 |
| CP2B03 | 116 | 37.068 | 23 | 32 | 116.618 | -23.532 | 290 | 460987 | 7397544 | 50 |
| CP2B04 | 116 | 34.838 | 23 | 32 | 116.581 | -23.538 | 281 | 457194 | 7396905 | 50 |
| CP2B05 | 116 | 35.395 | 23 | 34 | 116.590 | -23.568 | 289 | 458151 | 7393550 | 50 |
| CP2B06 | 116 | 36.944 | 23 | 36 | 116.616 | -23.604 | 297 | 460795 | 7389613 | 50 |
| CP2B07 | 116 | 37.434 | 23 | 39 | 116.624 | -23.645 | 314 | 461642 | 7384985 | 50 |
| CP2B08 | 116 | 39.695 | 23 | 40 | 116.662 | -23.670 | 323 | 465491 | 7382305 | 50 |
| CP2B09 | 116 | 40.363 | 23 | 42 | 116.673 | -23.707 | 338 | 466638 | 7378199 | 50 |
| CP2B10 | 116 | 38.914 | 23 | 45 | 116.649 | -23.750 | 354 | 464187 | 7373370 | 50 |
| CP2B11 | 116 | 39.315 | 23 | 46 | 116.655 | -23.773 | 374 | 464873 | 7370912 | 50 |
| CP2B12 | 116 | 37.919 | 23 | 49 | 116.632 | -23.813 | 398 | 462513 | 7366478 | 50 |
| CP2B13 | 116 | 36.503 | 23 | 51 | 116.608 | -23.847 | 444 | 460122 | 7362635 | 50 |
| CP2B14 | 116 | 34.564 | 23 | 52 | 116.576 | -23.874 | 410 | 456841 | 7359652 | 50 |
| CP2B15 | 116 | 33.967 | 23 | 55 | 116.566 | -23.915 | 400 | 455839 | 7355153 | 50 |
| CP2B16 | 116 | 30.959 | 23 | 56 | 116.516 | -23.927 | 382 | 450744 | 7353774 | 50 |
| CP2B17 | 116 | 28.824 | 23 | 57 | 116.480 | -23.953 | 372 | 447132 | 7350924 | 50 |
| CP2B18 | 116 | 28.353 | 23 | 60 | 116.473 | -23.997 | 364 | 446351 | 7343008 | 50 |
| CP2B19 | 116 | 27.891 | 24 | 2 | 116.465 | -24.034 | 354 | 445583 | 7341935 | 50 |
| CP2B20 | 116 | 27.178 | 24 | 4 | 116.453 | -24.074 | 350 | 444392 | 7337426 | 50 |
| CP2B21 | 116 | 27.191 | 24 | 7 | 116.453 | -24.118 | 344 | 444434 | 7332633 | 50 |
| CP2B22 | 116 | 26.585 | 24 | 10 | 116.443 | -24.169 | 390 | 443429 | 7326961 | 50 |
| CP2B23 | 116 | 26.768 | 24 | 12 | 116.446 | -24.205 | 400 | 443753 | 7322997 | 50 |
| CP2B24 | 116 | 24.611 | 24 | 14 | 116.410 | -24.234 | 394 | 440118 | 7319768 | 50 |
| CP2B25 | 116 | 22.863 | 24 | 16 | 116.381 | -24.261 | 377 | 437172 | 7316713 | 50 |
| CP2B26 | 116 | 20.219 | 24 | 17 | 116.337 | -24.279 | 377 | 432710 | 7314683 | 50 |
| CP2B27 | 116 | 17.625 | 24 | 18 | 116.294 | -24.304 | 391 | 428337 | 7311930 | 50 |
| CP2B28 | 116 | 17.765 | 24 | 20 | 116.296 | -24.341 | 370 | 428593 | 7307809 | 50 |
| CP2B29 | 116 | 18.072 | 24 | 23 | 116.301 | -24.384 | 347 | 429135 | 7303087 | 50 |
| CP2B30 | 116 | 17.632 | 24 | 26 | 116.294 | -24.429 | 328 | 428418 | 7298136 | 50 |
| CP2B31 | 116 | 17.101 | 24 | 28 | 116.285 | -24.472 | 315 | 427544 | 7293277 | 50 |
| CP2B32 | 116 | 15.212 | 24 | 30 | 116.254 | -24.508 | 321 | 424376 | 7289380 | 50 |
| CP2B33 | 116 | 13.415 | 24 | 33 | 116.224 | -24.545 | 302 | 421365 | 7285233 | 50 |
| CP2B34 | 116 | 12.730 | 24 | 35 | 116.212 | -24.579 | 301 | 420230 | 7281415 | 50 |
| CP2B35 | 116 | 11.135 | 24 | 37 | 116.186 | -24.615 | 286 | 417560 | 7277481 | 50 |
| CP2B36 | 116 | 10.084 | 24 | 40 | 116.168 | -24.666 | 280 | 415823 | 7271817 | 50 |
| CP2B37 | 116 | 9.261 | 24 | 42 | 116.154 | -24.703 | 300 | 414458 | 7267721 | 50 |
| CP2B38 | 116 | 6.822 | 24 | 43 | 116.114 | -24.725 | 315 | 410362 | 7265261 | 50 |
| CP2B39 | 116 | 4.255 | 24 | 44 | 116.071 | -24.739 | 299 | 406046 | 7263665 | 50 |
| CP2B40 | 116 | 1.873 | 24 | 45 | 116.031 | -24.756 | 280 | 402045 | 7261680 | 50 |
| CP2B41 | 116 | 0.550 | 24 | 43 | 116.009 | -24.787 | 274 | 399850 | 7257169 | 50 |
| CP2B42 | 115 | 58.392 | 24 | 49 | 115.973 | -24.824 | 251 | 396233 | 7254161 | 50 |
| CP2B43 | 115 | 56.743 | 24 | 52 | 115.946 | -24.861 | 240 | 393490 | 7250047 | 50 |
| CP2B44 | 115 | 56.920 | 24 | 54 | 115.949 | -24.904 | 240 | 393825 | 7245283 | 50 |

| Station | Long | | Lat | | Decimal Coordinates | | | | | |
|---|---|---|---|---|---|---|---|---|---|---|
| Station | (°) | (') | (°) | (') | Long (°) Longitude_dd | Lat (°) Latitude_dd | Elevation | Easting | Northing | Zone |
| CP2B45 | 115 | 58.432 | 24 | 56 | 115.974 | -24.939 | 247 | 396400 | 7241451 | 50 |
| CP2B46 | 115 | 57.892 | 24 | 59 | 115.965 | -24.978 | 253 | 395523 | 7237074 | 50 |
| CP2B47 | 115 | 57.906 | 25 | 1 | 115.965 | -25.024 | 238 | 395586 | 7231981 | 50 |
| CP2B48 | 115 | 57.682 | 25 | 3 | 115.961 | -25.056 | 244 | 395237 | 7228474 | 50 |
| CP2B49 | 115 | 58.311 | 25 | 6 | 115.972 | -25.098 | 249 | 396327 | 7223804 | 50 |
| CP2B50 | 115 | 8.302 | 25 | 8 | 115.961 | -25.138 | 271 | 395273 | 7219328 | 50 |
| CP2B51 | 115 | 55.587 | 25 | 10 | 115.926 | -25.170 | 239 | 391814 | 7215808 | 50 |
| CP2B52 | 115 | 54.061 | 25 | 13 | 115.901 | -25.209 | 238 | 389285 | 7211494 | 50 |
| CP2B53 | 115 | 54.467 | 25 | 15 | 115.908 | -25.249 | 247 | 390003 | 7207033 | 50 |
| CP2B54 | 115 | 51.152 | 25 | 18 | 115.853 | -25.293 | 243 | 384482 | 7202100 | 50 |
| CP2B55 | 115 | 52.135 | 25 | 16 | 115.869 | -25.273 | 244 | 386111 | 7204333 | 50 |
| CP3B01 | 116 | 40.103 | 25 | 16.017 | 116.668 | -25.267 | 358 | 466611 | 7205450 | 50 |
| CP3B02 | 116 | 39.547 | 25 | 18.340 | 116.659 | -25.306 | 367 | 465688 | 7201160 | 50 |
| CP3B03 | 116 | 39.666 | 25 | 20.663 | 116.661 | -25.344 | 370 | 465894 | 7196874 | 50 |
| CP3B04 | 116 | 39.195 | 25 | 23.391 | 116.653 | -25.390 | 377 | 465121 | 7191838 | 50 |
| CP3B05 | 116 | 38.324 | 25 | 25.292 | 116.639 | -25.422 | 387 | 463698 | 7188327 | 50 |
| CP3B06 | 116 | 39.184 | 25 | 27.589 | 116.653 | -25.460 | 397 | 465123 | 7184087 | 50 |
| CP3B07 | 116 | 38.785 | 25 | 30.140 | 116.646 | -25.502 | 426 | 464465 | 7179380 | 50 |
| CP3B08 | 116 | 41.081 | 25 | 31.767 | 116.685 | -25.529 | 414 | 468318 | 7176387 | 50 |
| CP3B09 | 116 | 40.716 | 25 | 34.005 | 116.679 | -25.567 | 396 | 467718 | 7172255 | 50 |
| CP3B10 part 1 | 116 | 40.045 | 25 | 36.481 | 116.667 | -25.608 | 390 | 466605 | 7167682 | 50 |
| CP3B10 part 2 | 116 | 40.045 | 25 | 36.481 | 116.667 | -25.608 | 390 | 466605 | 7167682 | 50 |
| CP3B11 | 116 | 39.224 | 25 | 38.445 | 116.654 | -25.641 | 379 | 465241 | 7164053 | 50 |
| CP3B12 | 116 | 38.344 | 25 | 40.503 | 116.639 | -25.675 | 376 | 463782 | 7160251 | 50 |
| CP3B13 | 116 | 37.438 | 25 | 42.791 | 116.624 | -25.713 | 363 | 462277 | 7156024 | 50 |
| CP3B14 | 116 | 37.948 | 25 | 45.500 | 116.632 | -25.758 | 361 | 463144 | 7151028 | 50 |
| CP3B15 | 116 | 37.755 | 25 | 48.154 | 116.629 | -25.803 | 352 | 462833 | 7146129 | 50 |
| CP3B16 | 116 | 38.963 | 25 | 50.612 | 116.649 | -25.844 | 364 | 464863 | 7141598 | 50 |
| CP3B17 | 116 | 40.382 | 25 | 52.882 | 116.673 | -25.881 | 365 | 467244 | 7137414 | 50 |
| CP3B18 | 116 | 40.987 | 25 | 54.635 | 116.683 | -25.911 | 350 | 468263 | 7134180 | 50 |
| CP3B19 | 116 | 39.272 | 25 | 57.009 | 116.655 | -25.950 | 345 | 465411 | 7129791 | 50 |
| CP3B20 | 116 | 37.488 | 25 | 59.357 | 116.625 | -25.989 | 342 | 462448 | 7125453 | 50 |
| CP3B21 | 116 | 36.328 | 26 | 1.936 | 116.605 | -26.032 | 334 | 460527 | 7120683 | 50 |
| CP3B22 | 116 | 36.107 | 26 | 4.644 | 116.602 | -26.077 | 331 | 460174 | 7115684 | 50 |

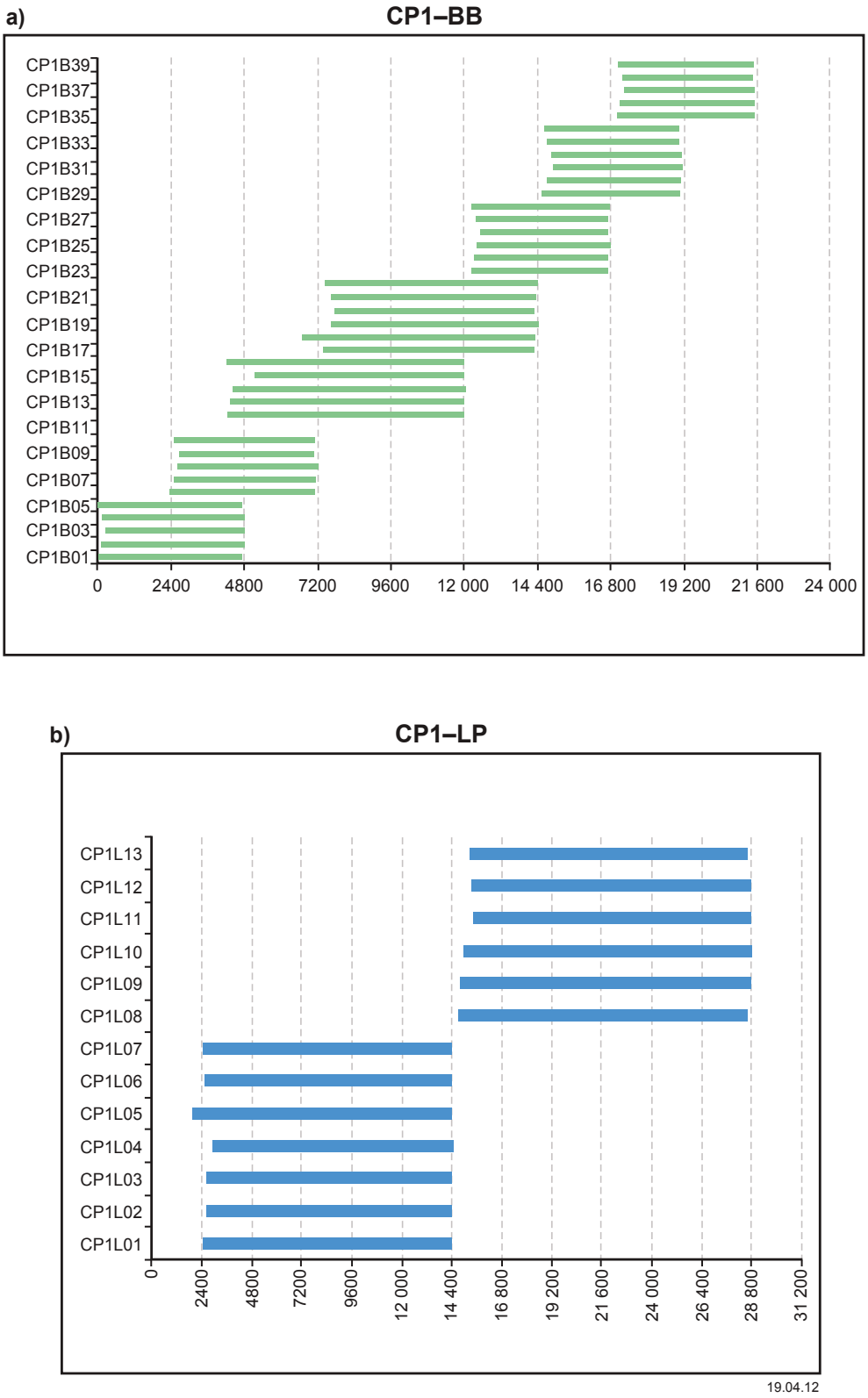


**Figure A1. Duration of deployment for line 10GA–CPI**

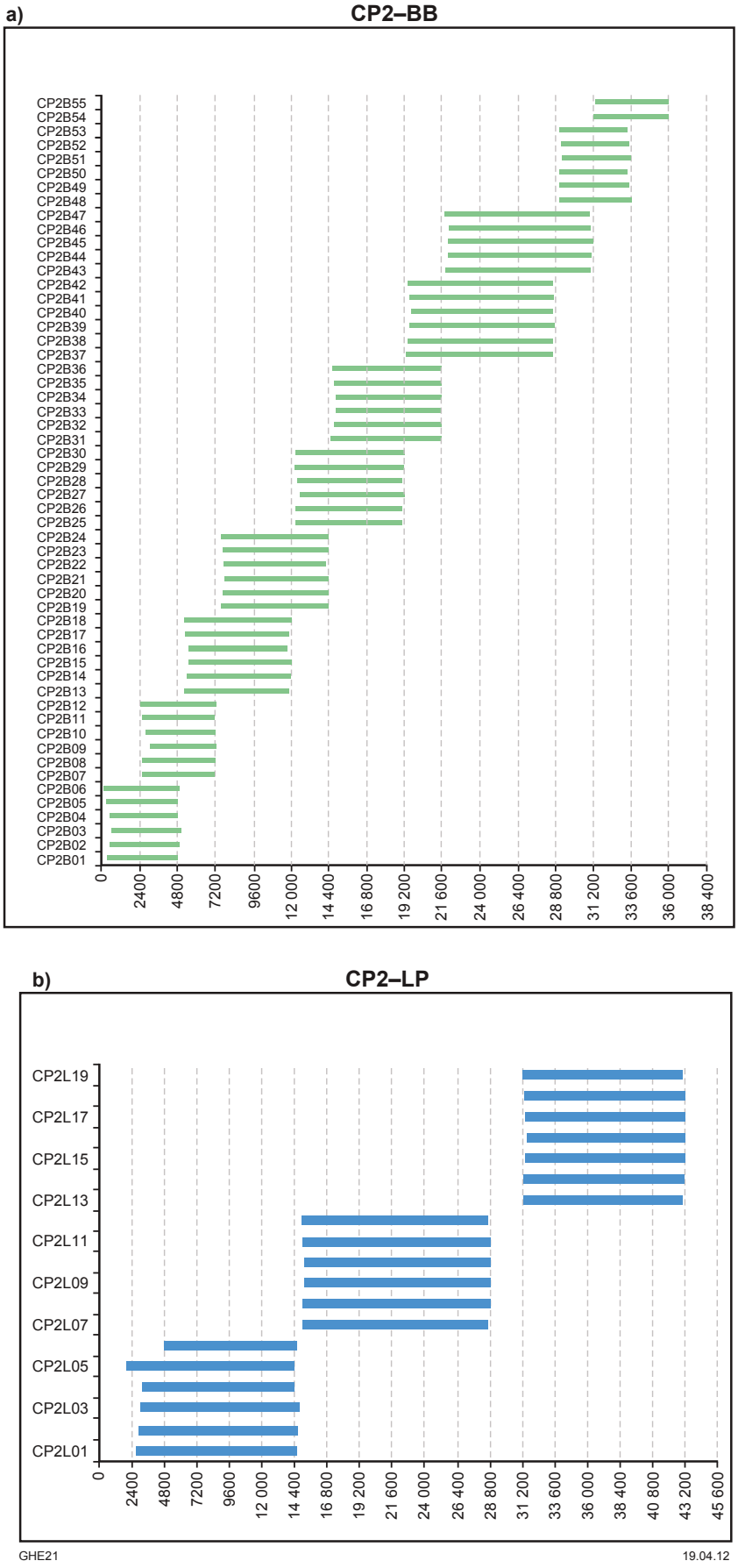


**Figure A2. Duration of deployments for line 10GA–CP2**

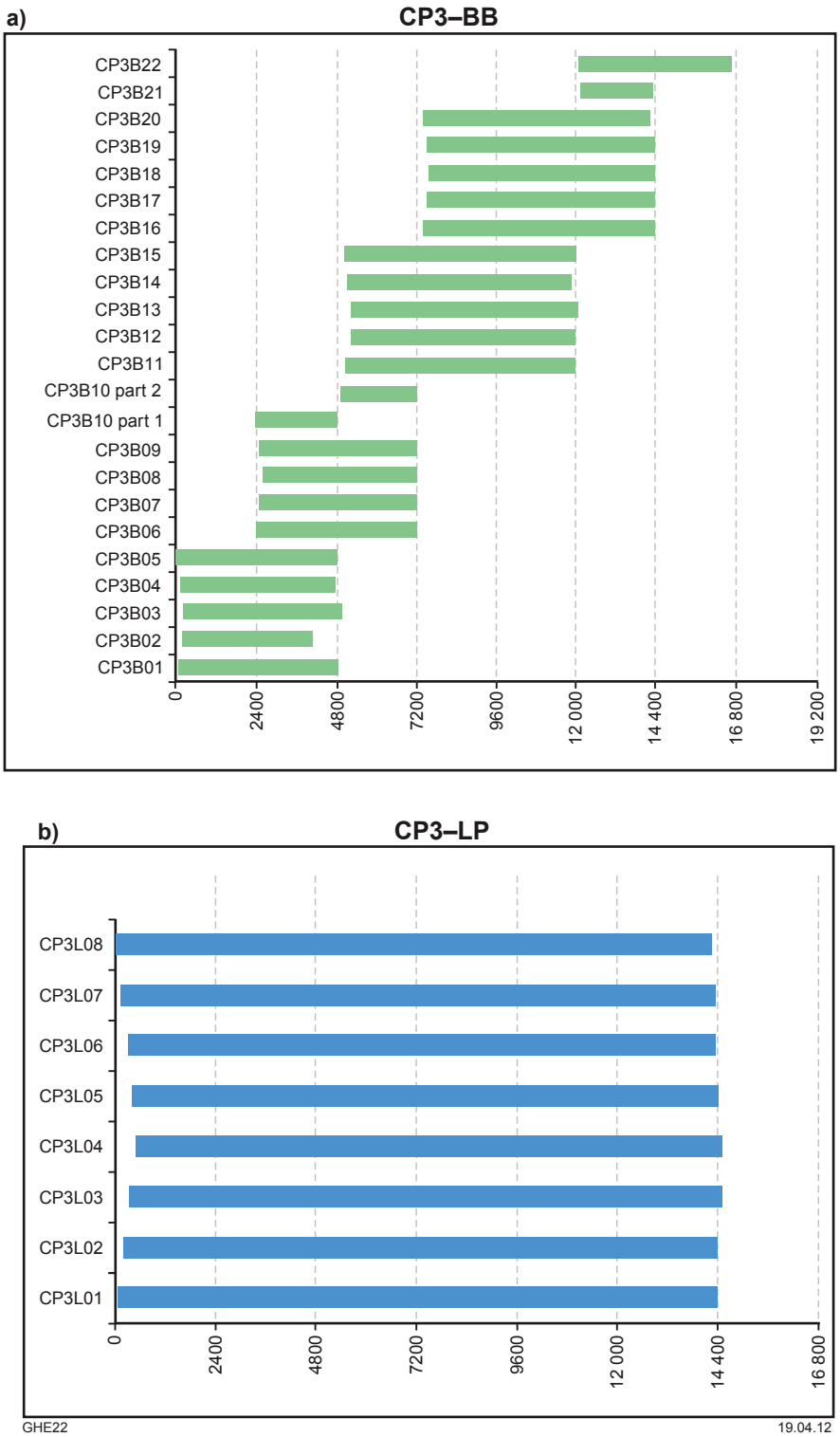


**Figure A3. Duration of deployments for line 10GA–CP3**